



A study of the relation between ocean storms and the Earth's hum

Junkee Rhie and Barbara Romanowicz

Seismological Laboratory, University of California, Berkeley, 209 McCone Hall, Berkeley, California 94720, USA
(rhie@seismo.berkeley.edu; barbar@seismo.berkeley.edu)

[1] We previously showed that the Earth's "hum" is generated primarily in the northern oceans during the northern hemisphere winter and in the southern oceans during the summer. To gain further insight into the process that converts ocean storm energy into elastic energy through coupling of ocean waves with the seafloor, we here investigate a 4-day-long time window in the year 2000 that is free of large earthquakes but contains two large "hum" events. From a comparison of the time functions of two events and their relative arrival times at the two arrays in California and Japan, we infer that the generation of the "hum" events occurs close to shore and comprises three elements: (1) short-period ocean waves interact nonlinearly to produce infragravity waves as the storm reaches the coast of North America; (2) infragravity waves interact with the seafloor locally to generate long-period Rayleigh waves; and (3) some free infragravity wave energy radiates out into the open ocean, propagates across the north Pacific basin, and couples to the seafloor when it reaches distant coasts northeast of Japan. We also compare the yearly fluctuations in the amplitudes observed on the two arrays in the low-frequency "hum" band (specifically at 240 s) and in the microseismic band (2–25 s). During the winter, strong correlation between the amplitude fluctuations in the "hum" and microseismic bands at BDSN is consistent with a common generation mechanism of both types of seismic noise from nonlinear interaction of ocean waves near the west coast of North America.

Components: 8173 words, 18 figures, 1 table.

Keywords: Hum of the Earth; microseisms; infragravity waves.

Index Terms: 4546 Oceanography: Physical: Nearshore processes; 4560 Oceanography: Physical: Surface waves and tides (1222); 7255 Seismology: Surface waves and free oscillations.

Received 9 February 2006; **Revised** 19 June 2006; **Accepted** 10 July 2006; **Published** XX Month 2006.

Rhie, J., and B. Romanowicz (2006), A study of the relation between ocean storms and the Earth's hum, *Geochem. Geophys. Geosyst.*, 7, XXXXXX, doi:10.1029/2006GC001274.

1. Introduction

[2] Since the discovery of the Earth's "hum" [Nawa *et al.*, 1998], seismologists have tried to determine the source of the continuous background free oscillations observed in low-frequency seismic spectra in the absence of earthquakes.

[3] In the last decade, some key features of these background oscillations have been documented. First, their source needs to be close to the Earth's surface, because the fundamental mode is preferentially excited [Nawa *et al.*, 1998; Suda *et al.*, 1998] and no clear evidence for higher mode excitation has yet been found. Second, these oscillations must be related to atmospheric processes,

44 because annual [Nishida *et al.*, 2000] and seasonal
 45 [Tanimoto and Um, 1999; Ekström, 2001] varia-
 46 tions in their amplitudes have been documented.
 47 Finally, they are not related to local atmospheric
 48 variations above a given seismic station, since
 49 correcting for the local barometric pressure fluc-
 50 tuations brings out the free oscillation signal in
 51 the seismic data more strongly [e.g., Roullet and
 52 Crawford, 2000].

53 [4] Early studies proposed that the “hum” could be
 54 due to turbulent atmospheric motions and showed
 55 that such a process could explain the corresponding
 56 energy level, equivalent to a M 5.8–6.0 earthquake
 57 every day [Tanimoto and Um, 1999; Ekström,
 58 2001]. However, no observations of atmospheric
 59 convection at this scale are available to confirm this
 60 hypothesis. In the meantime, it was suggested that
 61 the oceans could play a role [Watada and Masters,
 62 2001; Rhie and Romanowicz, 2003; Tanimoto,
 63 2003].

64 [5] Until recently, most studies of the “hum” have
 65 considered stacks of low-frequency spectra for
 66 days “free of large earthquakes. In order to gain
 67 resolution in time and space and determine whether
 68 the sources are distributed uniformly around the
 69 globe, as implied by the atmospheric turbulence
 70 model [e.g., Nishida and Kobayashi, 1999], or else
 71 have their origin in the oceans, it is necessary to
 72 adopt a time domain, propagating wave approach.
 73 In a recent study, using an array stacking method
 74 applied to two regional arrays of seismic stations
 75 equipped with very broadband STS-1 seismome-
 76 ters [Wielandt and Streckeisen, 1982; Wielandt and
 77 Stein, 1986], we showed that the sources of the
 78 “hum” are primarily located in the northern Pacific
 79 Ocean and in the southern oceans during the
 80 northern hemisphere winter and summer, respec-
 81 tively [Rhie and Romanowicz, 2004 (hereafter
 82 referred to as RR04)], following the seasonal
 83 variations in maximum significant wave heights
 84 over the globe, which switch from northern to
 85 southern oceans between winter and summer. We
 86 suggested that the generation of the hum involved a
 87 three stage atmosphere/ocean/seafloor coupling
 88 process: (1) conversion of atmospheric storm en-
 89 ergy into short-period ocean waves, (2) nonlinear
 90 interaction of ocean waves producing longer-
 91 period, infragravity waves, and (3) coupling of
 92 infragravity waves to the seafloor, through a pro-
 93 cess involving irregularities in the ocean floor
 94 topography. However, the resolution of our study
 95 did not allow us to more specifically determine
 96 whether the generation of seismic waves occurred

in the middle of ocean basins or close to shore [e.g.,
 97 Webb *et al.*, 1991; Webb, 1998]. The preferential
 98 location of the sources of the Earth’s “hum” in the
 99 oceans has now been confirmed independently
 100 [Nishida and Fukao, 2004; Ekström and Ekström,
 101 2005]. In a recent study, Tanimoto [2005] showed
 102 that the characteristic shape and level of the low-
 103 frequency background noise spectrum could be
 104 reproduced if the generation process involved the
 105 action of ocean infragravity waves on the ocean
 106 floor, and suggested that typically, the area involved
 107 in the coupling to the ocean floor need not be larger
 108 than about $100 \times 100 \text{ km}^2$. However, the linear
 109 process proposed may not be physically plausible,
 110 because of the difference in wavelength between
 111 infragravity and elastic waves (S. Webb, personal
 112 communication, 2006). 113

[6] On the other hand, oceanographers have long
 114 studied the relation between infragravity waves and
 115 swell. Early studies have documented strong cor-
 116 relation between their energy levels, which indicate
 117 that infragravity waves are driven by swell [e.g.,
 118 Munk, 1949; Tucker, 1950]. Theoretical studies
 119 have demonstrated that infragravity waves are
 120 second order forced waves excited by nonlinear
 121 difference frequency interactions of pairs of swell
 122 components [Hasselmann, 1962; Longuet-Higgins
 123 and Stewart, 1962]. A question that generated
 124 some debate was whether the observed infragravity
 125 waves away from the coast are “forced” waves
 126 bound to the short carrier ocean surface waves and
 127 traveling with their group velocity, or “free” waves
 128 released in the surf zone and subsequently reflected
 129 from the beach which, under certain conditions,
 130 may radiate into deep ocean basins [e.g., Sutton
 131 *et al.*, 1965; Webb *et al.*, 1991; Okihiro *et al.*, 1992;
 132 Herbers *et al.*, 1994, 1995a, 1995b]. In particular,
 133 Webb *et al.* [1991] found that infragravity wave
 134 energy observed on the seafloor away from the
 135 coast was correlated not with the local swell wave
 136 energy but with swell energy averaged over all
 137 coastlines within the line of sight of their experi-
 138 mental sites, in the north Atlantic Ocean and off-
 139 shore southern California. 140

[7] Recently, we analyzed the relation between
 141 ocean storms off-shore California and infragravity
 142 wave noise observed on several broadband seafloor
 143 stations in California and Oregon [Dolenc *et al.*,
 144 2005a]. We also found that the seismic noise
 145 observed in the infragravity wave band correlates
 146 with significant wave height as recorded on re-
 147 gional ocean buoys, and marks the passage of the
 148 storms over the buoy which is closest to the shore.
 149

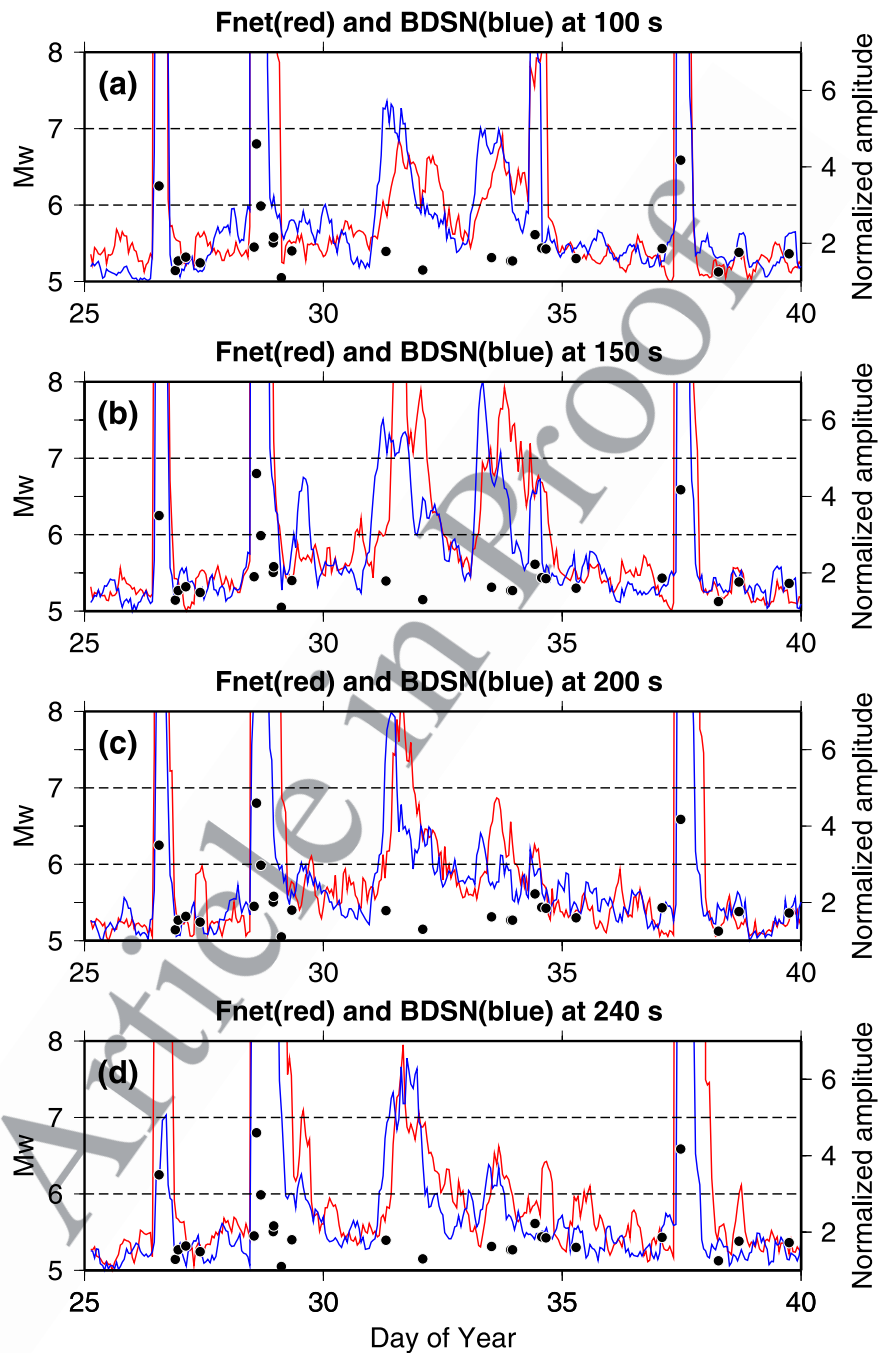


Figure 1. (a) Maximum stack amplitude (MSA, see definition in text) filtered using a Gaussian filter with center period of 100 s for BDSN (blue) and F-net (red), normalized by minimum value of MSA for a given time window. The linear scale on the y axis to the right is used for the normalized MSA to more clearly see the variations in amplitude of the background noise. Black dots represent earthquakes which occurred during the period considered. The corresponding scale is logarithmic (moment magnitude) and is given on the y axis to the left. (b–d) Same as Figure 1a for 150, 200, and 240 s.

150 More recent results based on data from an ocean
151 floor station further away from shore [Dolenc *et*
152 *al.*, 2005b] indicate that the increase in amplitude
153 in the infragravity frequency band (50–200 s)
154 associated with the passage of a storm occurs when

the storm reaches the near coastal buoys, and not
155 earlier, when the storm passes over the seismic
156 station. This implies that pressure fluctuations in
157 the ocean during the passage of the storm above the
158

Table 1. $M_w > 5.0$ Earthquake Catalog From 25 January to 9 February in 2000 From NEIC

Date	Time	Latitude	Longitude	Depth	Mag.
2000/01/25	16:43:22.95	27.6630	92.6310	33.0	5.20
2000/01/26	13:26:50.00	-17.2720	-174.0020	33.00	6.30
2000/01/26	21:37:57.77	30.9730	95.5020	33.00	5.20
2000/01/26	23:00:19.94	40.0210	52.9010	33.00	5.30
2000/01/26	23:34:04.50	-23.7220	-66.4770	221.60	5.00
2000/01/27	02:49:44.91	-34.8070	-105.4590	10.00	5.40
2000/01/27	10:10:57.25	31.6780	141.6860	33.00	5.30
2000/01/28	08:49:30.87	7.4570	-77.8500	21.40	5.40
2000/01/28	13:17:52.87	-7.4850	122.6780	574.90	5.50
2000/01/28	14:21:07.34	43.0460	146.8370	61.10	6.80
2000/01/28	16:39:24.28	26.0760	124.4960	193.90	6.00
2000/01/28	17:57:00.55	14.4350	146.4620	45.20	5.20
2000/01/28	22:42:26.25	-1.3470	89.0830	10.00	5.50
2000/01/28	22:57:51.70	-9.6910	118.7640	83.40	5.60
2000/01/29	02:53:54.89	4.8570	126.2590	100.00	5.10
2000/01/29	05:48:10.77	-20.5630	-178.2880	562.90	5.00
2000/01/29	08:13:10.73	-8.6330	111.1370	60.70	5.40
2000/01/31	07:25:59.74	38.1140	88.6040	33.00	5.40
2000/02/01	00:01:05.42	-4.3580	151.9070	189.00	5.20
2000/02/01	02:00:10.68	13.0100	-88.8470	55.00	5.20
2000/02/02	12:25:21.92	-49.0240	124.9790	10.00	5.40
2000/02/02	21:58:49.71	-5.7300	148.9320	112.80	5.30
2000/02/02	22:58:01.55	35.2880	58.2180	33.00	5.30
2000/02/03	10:24:57.77	65.0087	-154.2390	10.00	5.98
2000/02/03	13:42:25.04	13.5720	121.5460	33.00	5.50
2000/02/03	15:53:12.96	75.2710	10.1950	10.00	5.50
2000/02/04	07:02:11.39	-40.6310	-85.9180	10.00	5.30
2000/01/25	16:43:22.95	27.6630	92.6310	33.0	5.20
2000/02/06	02:08:07.14	1.2950	126.2720	33.00	5.50
2000/02/06	11:33:52.28	-5.8440	150.8760	33.00	6.60
2000/02/07	06:34:49.67	43.3680	147.4330	61.50	5.20
2000/02/07	16:41:04.58	31.0370	141.6940	33.00	5.40
2000/02/08	18:01:27.18	-21.9360	170.0680	33.00	5.40
2000/02/09	04:28:00.48	-16.6660	-172.6960	33.00	5.20
2000/02/09	09:33:54.05	-30.1050	-178.1130	56.70	5.00
2000/02/09	18:40:37.83	-27.6220	65.7240	10.00	5.10

station can be ruled out as the direct cause of the low-frequency seismic noise.

[8] In this paper, we investigate these processes further in an attempt to better understand where the coupling between infragravity waves and ocean floor occurs, generating the seismic “hum.” In particular, we describe in detail observations made during one particular time period of unusually high levels of low-frequency noise. We also present comparisons of the observed low-frequency seismic “hum” with noise in the microseismic frequency band (2–25 s), and discuss the relation between the two phenomena.

2. Earthquake “Free” Interval 2000.031–034

[9] In our previous study [RR04], we extracted time intervals which were not contaminated by

earthquakes, using strict selection criteria based on event magnitude. This significantly limited the number of usable days in a given year. For example, only 64 days of “earthquake free” data were kept for the year 2000. Among these, we identified the time interval 2000.030 to 2000.034 (i.e., 30 January to 3 February) as a particularly long interval free of large earthquakes, during which the background noise amplitude was unusually high, and during which two large noise events were observed, that could be studied in more detail.

[10] As described in RR04, we considered data at two regional arrays of very broadband seismometers, BDSN (Berkeley Digital Seismic Network) in California, and F-net in Japan. For each array, we stacked narrow-band filtered time domain vertical component seismograms according to the dispersion and attenuation of Rayleigh waves, assuming plane wave propagation from an arbitrary azimuth. Here, we apply a 6 hour running average with a

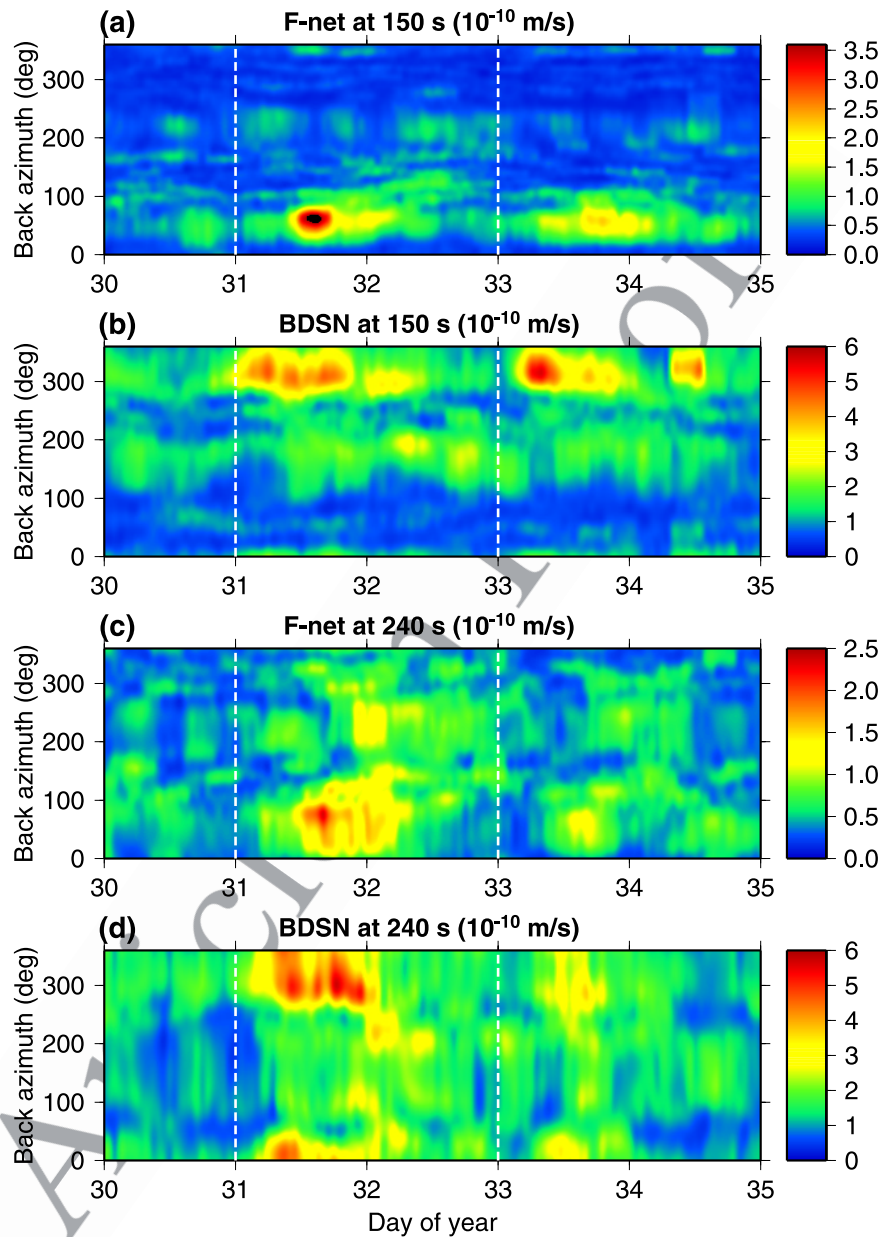
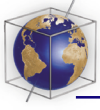


Figure 2. (a) Mean stack amplitude averaged over 6 hour sliding window (window shifted 1 hour between resolutions) as a function of time and back azimuth for F-net. A Gaussian filter with center period of 150 s was applied before stacking. (b) Same as Figure 2a for BDSN. (c) Same as Figure 2a for center period of 240 s. (d) Same as Figure 2c for BDSN. The time difference between corresponding energy arrivals at the two arrays on day 31 is about 8–10 hours, with F-net lagging behind BDSN. This is more clearly seen in the shorter-period plot.

196 time step of 1 hour to the stacked data at BDSN
197 and F-net respectively. At each time step, the stack
198 amplitude has a maximum corresponding to a
199 particular back-azimuth. We consider the resulting
200 maximum stack amplitudes (MSA) as a function of
201 time. We show in Appendix A that the level of the
202 background “hum” is consistent with previous
203 estimates [e.g., *Tanimoto and Um, 1999; Ekström,*
204 *2001*].

[11] We consider the 15 day period 2000.25 to 205
2000.40. In Figure 1, we plot the MSA as a 206
function of time in four different period bands. 207
We here use a linear scale for the MSA (different 208
from Figure A1) to more clearly see the variations 209
in amplitude of the background noise. We note the 210
well defined signature of large earthquakes, which 211
have a sharp onset, a slower decay and a relatively 212
sharp end. At the time resolution considered here, 213
this onset is practically coincident at both arrays. 214

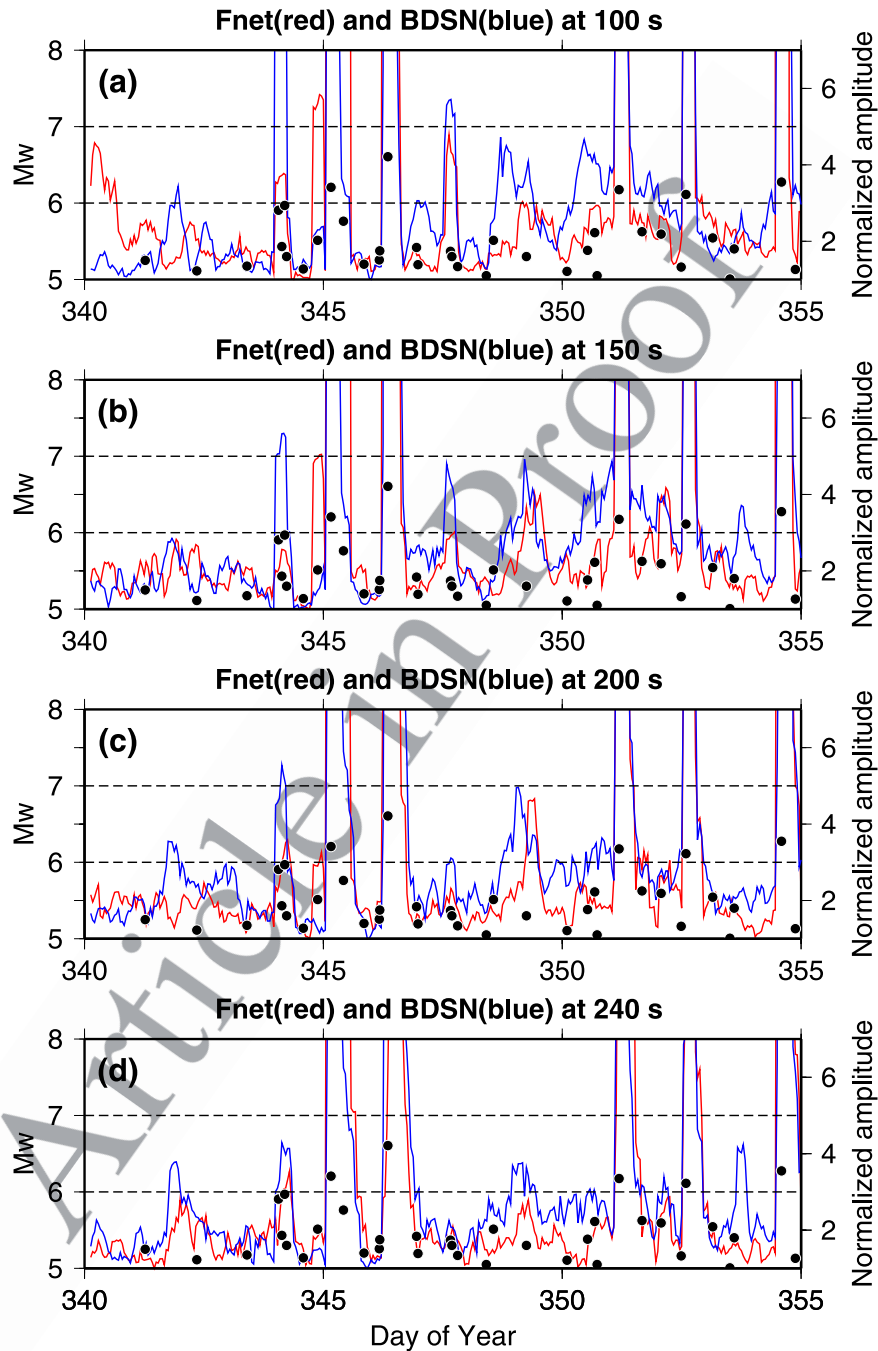
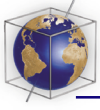


Figure 3. Same as Figure 1 for days from 340 to 355 in 2002.

215 The duration of the earthquake signal increases
216 with the size of the earthquake and is typically on
217 the order of 0.5 day for M_w 6 and 1–1.5 day for M_w
218 7 earthquakes, after which the signal drops below
219 the average background noise level. This is con-
220 sistent with what one expects from the decay of
221 Earth circling mantle Rayleigh waves generated by
222 large earthquakes.

223 [12] Table 1 lists all earthquakes larger than M 5.0
224 during these 15 days, as reported in the NEIC

catalog. During the time interval 2000.031 to 225
2000.034, there are no earthquakes larger than 226
M 5.5, yet the background noise rises well above 227
the noise floor, forming two particularly long 228
events, with a very different signature from that of 229
earthquakes: the rise time is longer, the decay very 230
slow and the ratio of the duration of each event to its 231
maximum amplitude, significantly larger. These 232
two noise events are observed on both arrays (i.e., 233
in California and in Japan), and there is a lag time of 234

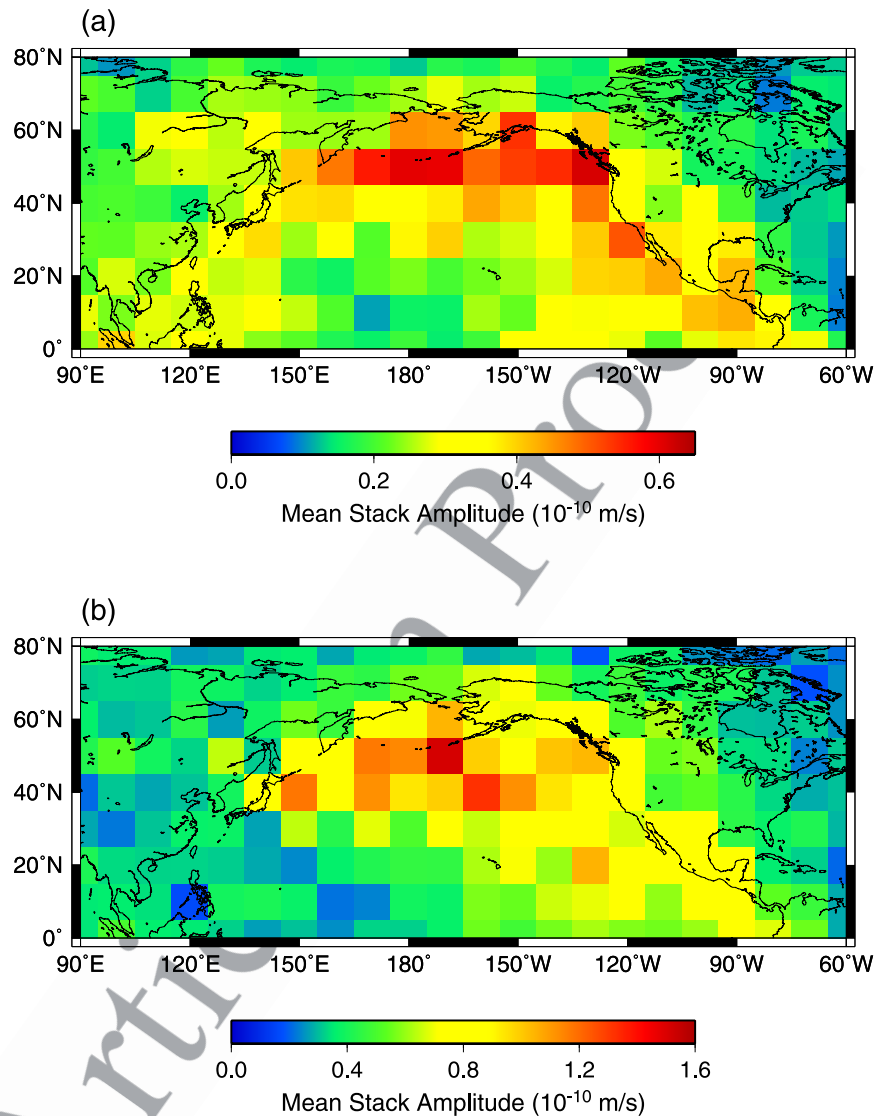


Figure 4. (a) Results of grid search method to locate the source of continuous long-period Rayleigh waves on 31 January 2000. Six hour waveforms Gaussian filtered with center period of 100 s from F-net, BDSN, and 10 European stations are used. Color indicates the mean stack amplitude over a 6 hour time window (2000.031,14:00–2000.031,20:00 UTC) after correcting waveforms at individual stations for attenuation and dispersion. (b) Same as Figure 4a for 150 s.

235 several hours between the two arrays. The second
236 event is weaker at the longest periods. We verify
237 that the back-azimuth corresponding to the maxi-
238 mum amplitude is very stable during these two
239 events, as illustrated in Figure 2, which also empha-
240 sizes the delay of about 8–10 hours between the
241 main energy arrivals at BDSN and F-net. We will
242 discuss these events in detail in what follows.

243 [13] This particular “earthquake free window” is
244 unique in that it lasts several days, and the noise
245 events are large. However, noise events with simi-
246 lar characteristics are observed at other times as

247 well. For example, Figure 3 shows a similar plot
248 for the time period 2002.340 to 2002.355, in which
249 we observe a noise event beginning on day
250 2002.349, showing similar time evolution as for
251 the events in 2000 described above: a slow rise
252 time and lag of ~ 8 –10 hours between the two
253 arrays. It is followed by a second noise event of
254 similar characteristics, but partially hidden behind
255 an earthquake of $M_w > 6$. In what follows, we
256 return to the time period 2000.031–034 for further
257 analysis.

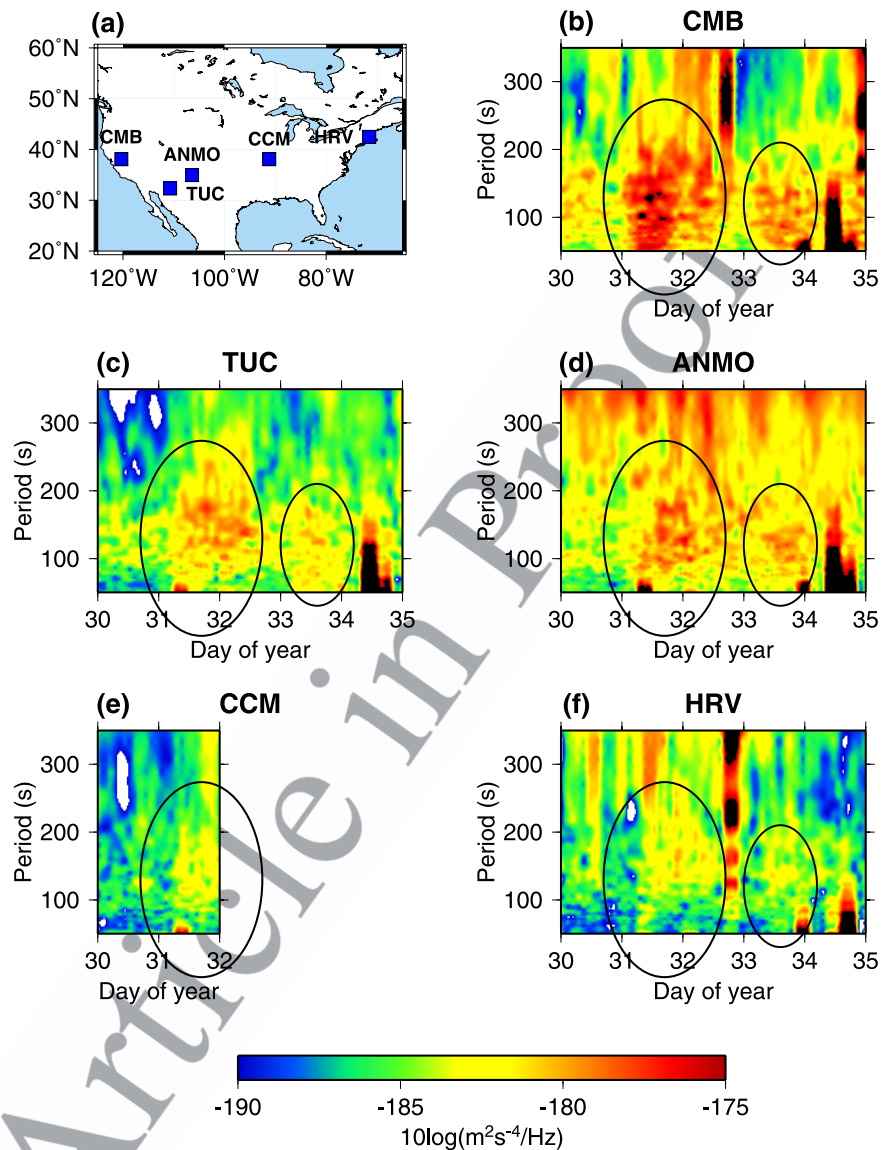


Figure 5. (a) Locations of five quiet seismic stations in North America. (b) Power spectral density (PSD) at CMB. It is clear that two large seismic energy arrivals (highlighted with black circles) are present on days 031 and 033. (c–f) Same as Figure 5b for TUC, ANMO, CCM, and HRV, respectively. For CCM the data are missing after day 33 through day 35. Large amplitude signals for periods <120 s on days 34 and 35 correspond to earthquakes (see Table 1).

258 [14] The large noise events observed on days
259 2000.031 and 2000.033 after applying a smoothing
260 moving average to the MSA, are the coalescence of
261 multiple smaller events, which, as we showed
262 previously, propagate across the two arrays with
263 the dispersion characteristics of Rayleigh waves
264 (see Figure 1 in RR04). In order to locate the
265 sources of these disturbances in RR04, we applied
266 a back-projection grid-search method to the origi-
267 nal time series, after band-pass filtering between
268 150–500 s, over a 6 hour period containing the
269 maximum stack amplitude on day 2000.031. We
270 showed that the sources of Rayleigh waves that

best fit the amplitudes observed both at BDSN and 271
F-net are located in the North Pacific Ocean basin. 272
We here apply the same back-projection method, 273
but using a narrow band filter centered at 150 and 274
100 s respectively, and obtain a band of source 275
locations which follows the north Pacific shoreline, 276
as illustrated in Figure 4. This is particularly clear 277
at 100 s. 278

[15] In order to obtain a stable solution using the 279
grid search method, it is necessary to process a 280
time interval of length about 6 hours, indicating 281
that many of the small events which compose the 282

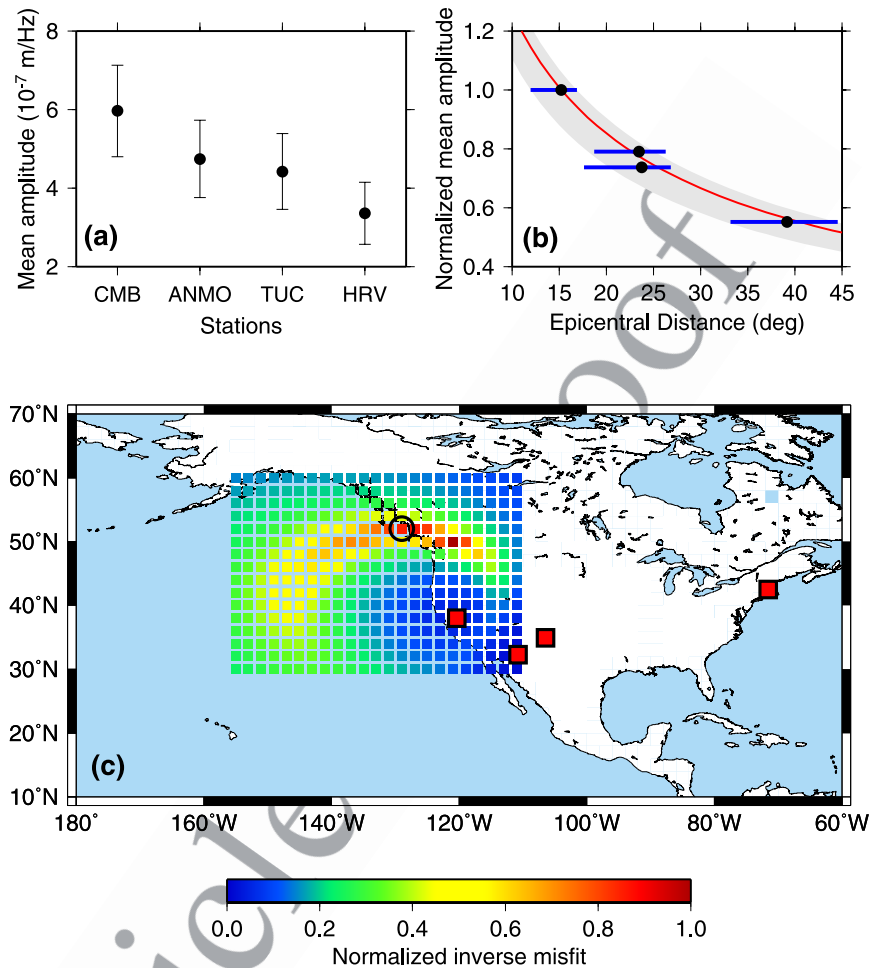


Figure 6. (a) Mean amplitude estimates and corresponding errors at stations considered in Figure 5. Error is estimated by random perturbation of time (± 6 hour) and period (± 30 s) window used for averaging. (b) Normalized observed mean amplitudes (black dots) and the theoretical attenuation curve (red) for the seismic source location indicated by a circle in Figure 6c. Gray shaded region and horizontal blue bars indicate the possible range of theoretical attenuation curves and epicenters from stations giving the good fit (i.e., normalized inverse misfit > 0.7). (c) Results of grid search for the location of the source of PSD noise highlighted in Figure 5. The PSD amplitudes were corrected for attenuation and geometrical spreading. The color scale represents the normalized inverse of the misfit between observed and predicted amplitudes (this way, the minimum misfit is always equal to 1). The circle indicates the off-shore location with small misfit.

283 larger noise event on day 2000.031 are too small to
 284 be studied individually, at least with this method:
 285 the minimum duration of the time window necessary
 286 to obtain a stable result is controlled by the
 287 available signal/noise ratio in the stacks. Here we
 288 show that the large “composite” event, obtained
 289 when using the 6 hour moving average, propagates
 290 west to east across the whole North American
 291 continent, with an amplitude decay consistent with
 292 the propagation of Rayleigh waves. Instead of
 293 stacking the noise data over an array of broadband
 294 seismic stations, we here consider five quiet
 295 broadband stations in North America, and, for
 296 each of them, we compute power spectral density

(PSD) as a function of time, with a 6 hour moving
 297 window and a 1 hour lag (Figure 5). All five
 298 stations show an increase in background noise
 299 during days 31–32, and another one, with smaller
 300 amplitude and narrower frequency range, on day 33
 301 (except for CCM for which data are not available on
 302 that day). Figure 6a compares the mean Fourier
 303 amplitudes at stations CMB, TUC, ANMO and
 304 HRV, averaged over the period range 100–200 s
 305 and time range 2000.31,00:00 and 2000.32,06:00.
 306 We chose this period range, because at lower
 307 frequencies, the background noise is dominated
 308 by site effects at some of the stations. From the
 309 amplitude decay it is possible to obtain a very rough
 310

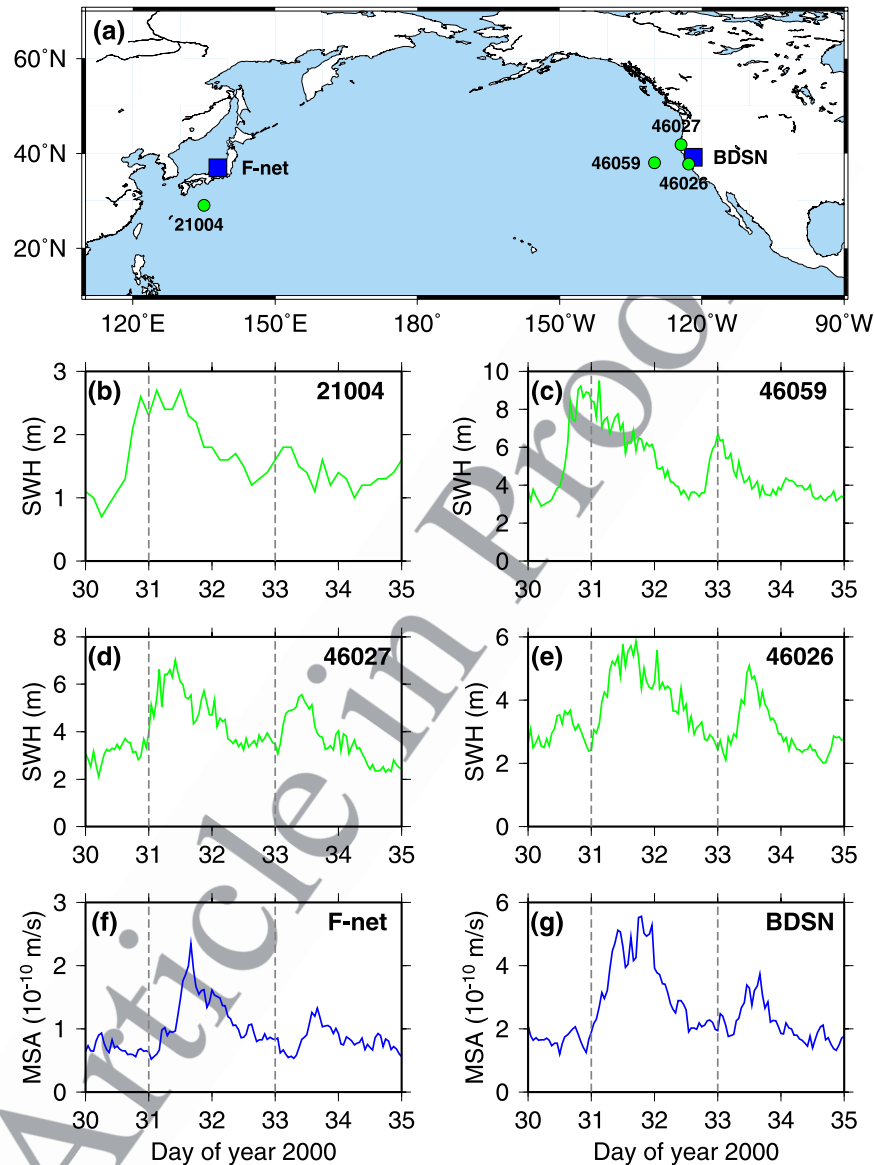


Figure 7. (a) Location of the two seismic arrays (blue squares) and ocean buoys (green dots). (b) Significant wave height recorded at buoy 21004. (c–e) Same as Figure 7b for buoys 44059, 46027, and 46026. (f) Maximum stack amplitude (MSA) Gaussian filtered with center period of 240 s recorded at F-net. (g) Same as Figure 7f for BDSN. Peaks in ocean wave data at off-shore buoys (21004 and 46059) arrive earlier than seismic peaks. For BDSN, arrival times of seismic energy are closer to those of the ocean wave peaks at buoys near the coast (46027 and 46026). The events arrive latest on F-net. Note that the MSA is also lower at F-net than at BDSN, consistent with more distant sources.

311 estimate of the location of the source of Rayleigh
312 waves by forward amplitude modeling. The results
313 are shown in Figure 6c, using CMB, TUC, ANMO
314 and HRV. Because the available azimuth range is
315 not very wide, there is a large uncertainty in the
316 longitude of the inferred source. However, it is
317 compatible with a location near the west coast of
318 North America. Figure 6b compares the observed
319 and predicted average Fourier amplitudes at four
320 stations. The amplitudes are normalized to those of

the most western station (CMB) and the predicted
amplitudes are computed assuming the Q model of
PREM for Rayleigh waves [Dziewonski and
Anderson, 1981] and accounting for geometric
spreading.

3. Correlation With Ocean Buoy Data 326

[16] To further investigate the origin of the noise
events on days 2000.031 and 2000.033, we now

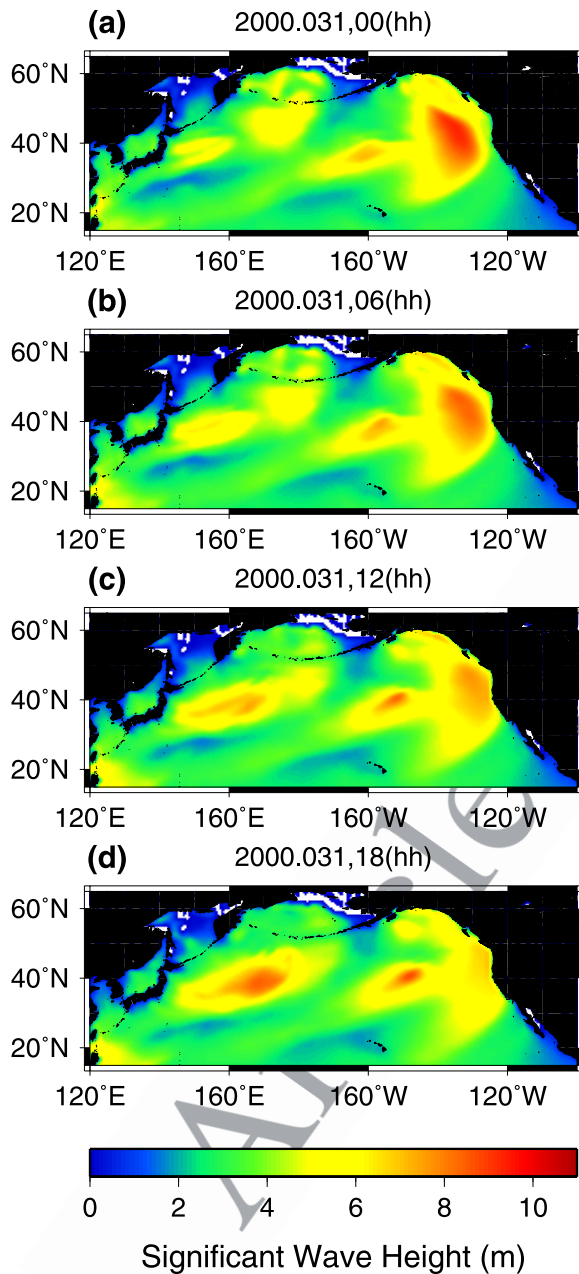


Figure 8. Significant wave height map on 31 January 2000 for the north Pacific Ocean, based on WAVEWATCH III. (a–d) Different time windows from 0 to 18 hour with 6 hour interval.

329 turn to a comparison with ocean buoy data. We
330 collected significant wave height (SWH) data measured
331 at buoys deployed in the north Pacific by the
332 National Ocean and Atmospheric Administration
333 (NOAA) and the Japan Meteorological Agency
334 (JMA) and operational during those days. We
335 compare SWH time series for this time period to
336 the time evolution of the maximum stack amplitudes
337 at BDSN and F-net for the same time

interval. Figure 7 shows such a comparison for 338
buoys located near Japan and near the California 339
coast. The time series on all buoys closely resemble 340
the “source signature” on the seismic stacks, 341
shown here at a period of 240 s. This is the case for 342
the event on 2000.031 as well as for the smaller 343
one on 2000.033. The seismic noise events on 344
BDSN lag those observed on buoy 46059 by about 345
10–12 hours, but are more or less coincident (to 346
within 1 hour, which is the minimum resolution of 347
these plots) with the events observed on the near 348
shore buoys, indicating that the location of the 349
coupling between ocean waves and the seafloor 350
occurs somewhere between buoy 46059 and the 351
shore, which is consistent with the results of 352
Figure 6c. The ocean storm which generated the 353
short-period waves observed on buoys both near 354
Japan and near the western US moved from east 355
to west across the north Pacific basin. Unfortunately, 356
we could not find any buoy data closer to 357
the eastern coast of Japan, or in other parts of the 358
western Pacific Ocean. To further investigate the 359
source of these waves, we therefore turn to wave 360
models. Figure 8 shows snapshots of the evolution 361
of wave height in the northern Pacific for day 362
2000.031, from the WAVEWATCH III model 363
[Tolman, 1999]. During that day, a large storm 364
arrives from the west toward the coast of California 365
and Oregon. It reaches the coast, according 366
to the model, between 6h and 12h on day 367
2000.031. It is followed by a smaller “tail,” about 368
3000 km behind, which, in turn, according to the 369
WAVEWATCH III model, reaches the coast between 370
0h and 6h on day 2000.033 (not shown). 371
The following storm system, which forms in the 372
western part of the north Pacific (around longitude 373
160°E on Figure 8) on day 2000.031 develops 374
into a stronger storm over the next few days. 375
This can be seen in the animation provided by 376
NOAA at <http://ursus-marinus.ncep.noaa.gov/history/waves/nww3.hs.anim.200001.gif> and 377
<http://ursus-marinus.ncep.noaa.gov/history/waves/nww3.hs.anim.200002.gif>. This storm is not associated 379
with any significantly increased seismic 380
noise on BDSN or F-net (Figure 1). Notably however, 381
in contrast to the previous one, this storm does 382
not reach the California coast, but dissipates in the 383
middle of the ocean. The distribution of wave 384
heights on Figure 8, together with the observation 385
of the significant delay in the stack energy at F-net 386
with respect to the BDSN (see also Figure 2), leads 387
us to propose the following sequence of events. 388
389

[17] On day 2000.031, a large storm, which developed 390
two days earlier in the middle of the north 391

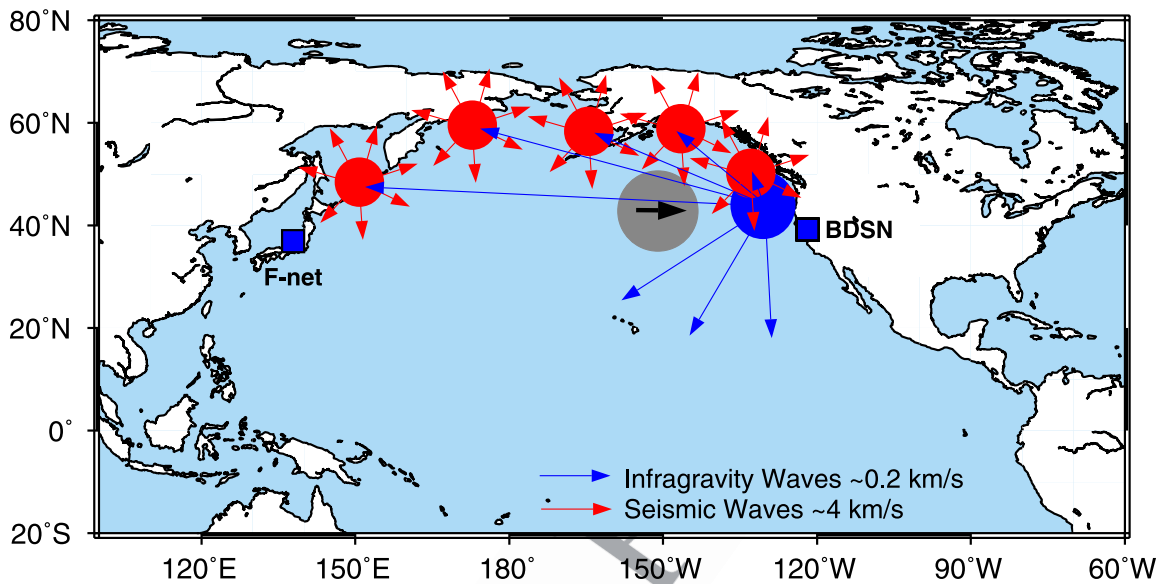


Figure 9. A schematic plot of the mechanism of conversion of energy from storm-related ocean surface waves to seismic waves. Gray circle indicates the moving storm, and blue and red circles (arrows) represent the source regions (radiation) of infragravity and seismic waves, respectively.

392 Pacific basin (according to wave models and buoy
393 data) and moving eastward toward North America,
394 reaches the vicinity of the western United States
395 coast. A second storm, weaker, but with similar
396 characteristics, follows by about 2 days. The seis-
397 mic background noise observed on the BDSN and
398 F-net arrays has the same amplitude signature, as a
399 function of time, as the storms. The process that
400 converts the storm energy into seismic energy,
401 which then propagates as Rayleigh waves, in par-
402 ticular through the North American continent,
403 appears to involve several steps (Figure 9): when
404 the storm approaches the US coast with its rough
405 seafloor topography, short-period ocean waves in-
406 teract nonlinearly to produce infragravity waves.
407 Part of the infragravity wave energy then converts
408 to seismic waves locally, to produce the background
409 noise event observed on BDSN, and part is
410 reflected back out to the ocean and travels across
411 the Pacific basin, in agreement with oceanographic
412 studies of the generation of infragravity waves [e.g.,
413 Munk *et al.*, 1964; Elgar *et al.*, 1992; Herbers *et*
414 *al.*, 1995a, 1995b]. We estimate that, at ~220 m/s,
415 “free” infragravity waves propagate about 6000–
416 8000 km in 8–10 hours. Consistent with the back-
417 azimuth of the maximum arrival of energy, the
418 conversion from infragravity waves to seismic
419 waves detected on F-net primarily occurs in the
420 vicinity of the western Aleutian arc. We note that
421 the absolute level of MSA is larger at BDSN than at
422 F-net (e.g., Figures 2 and 7), in agreement with the

inference that the source for F-net should be com- 423
paratively more distant and also weaker. 424

[18] We infer that free infragravity waves play a 425
role in generating the seismic disturbances in Japan 426
because of the 8–10 hour time delay between stack 427
maxima on BDSN and F-net. This is consistent 428
with observations of remotely generated infragrav- 429
ity waves [e.g., Herbers *et al.*, 1995a]. This time 430
delay is too short for propagation of short-period 431
ocean waves (and also “bound” infragravity 432
waves) from the center of the north Pacific basin, 433
and much too long for propagation of seismic 434
waves from a source near the US coast to Japan. 435
An alternative scenario for the sources of seismic 436
noise on F-net could involve the storm which 437
forms on the Japan side of the Pacific in the middle 438
of day 2000.031 (Figure 8). However, we rule this 439
out, because this storm intensifies only later and 440
reaches its peak around 03h on day 2000.032, 441
which is much later than the long-period seismic 442
peak on F-net. 443

[19] We note that the generation of large infragrav- 444
ity waves from short-period ocean waves along the 445
east coast of the Pacific (Canada, US) rather than 446
the west coast (Japan) is due to the fact that 447
prevailing winds are westerlies, and therefore most 448
ocean waves are driven from the west to the east, 449
interacting nonlinearly only with the coasts on the 450
east side of ocean basins. 451

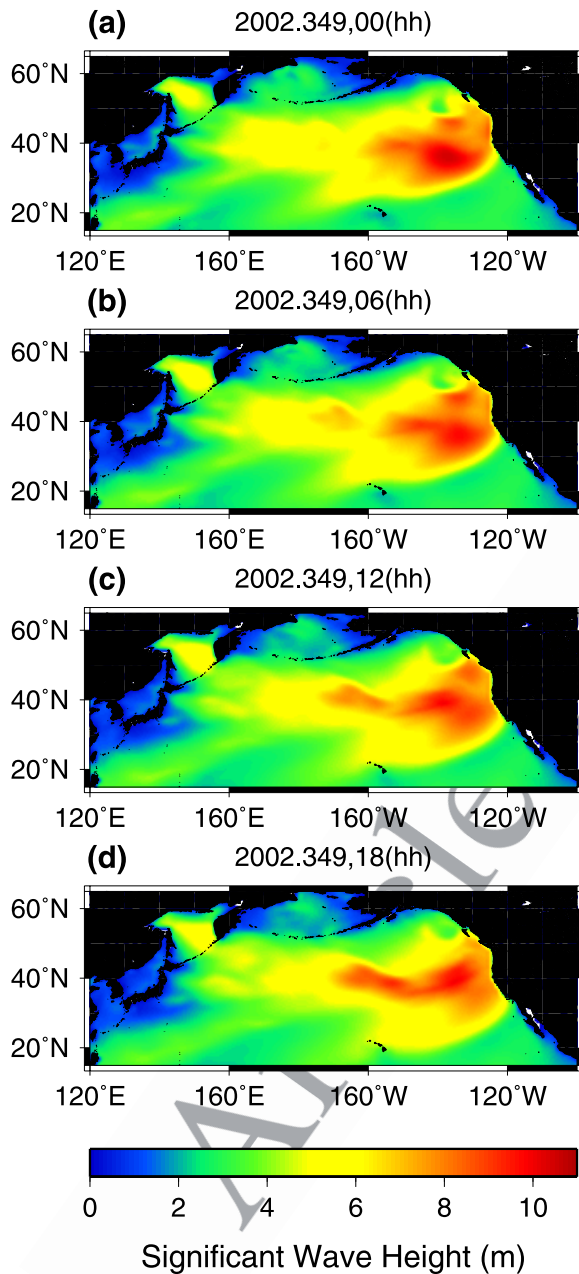


Figure 10. Significant wave height map on 15 December 2002 based on WAVEWATCH III. (a–d) Different time windows from 0 to 18 hour with 6 hour interval.

452 [20] In summary, the seismic sources that form the
453 composite events on days 2000.031 and 2000.033
454 are distributed around the Pacific, both in time and
455 space, but have a common cause: a strong storm
456 system which “hits” the North American coast
457 broadside. A similar type of storm which reaches
458 North America from the west, occurs on day
459 2002.349 (Figure 10), causing the disturbances
460 observed on Figure 3. We infer that the efficiency

of generation of seismic waves is particularly high 461
for these storms, due to their direction of approach 462
to the North American coast, and the fact that these 463
storms actually reach the coast. This is why we can 464
observe these remarkable “noise events” on the 465
stacks at BDSN and F-net so clearly. We have 466
evidence of directionality of the process, in that 467
station COL (Alaska) does not show any increase 468
of seismic noise in the 70–250 s pass band during 469
the same time period. At least, it is below detection 470
level by our methodology involving PSD spectra, 471
even though there is an indication, from the noise 472
in the microseismic bandpass (2–25 s) of a storm 473
reaching the Alaska coast nearby at the end of day 474
2000.031 (Figure 11). Such directionality would 475
also explain why we can so clearly follow the 476
particular seismic disturbance on day 2000.031 477
across North America. 478

[21] Other north Pacific storms must also generate 479
long-period seismic noise, however, the 480
corresponding noise “events” cannot often be 481
identified as clearly because they are either hidden 482
behind large seismic events, or do not have suffi- 483
cient amplitude levels to rise above the average 484
noise level on the two seismic arrays considered. 485
We note that many winter storms never reach the 486
north American coast, or turn further north into the 487
Gulf of Alaska. A systematic analysis of storm 488
characteristics in the north Pacific in relation to the 489
“hum” is beyond the scope of this paper and will 490
be addressed in a further study. 491

4. Comparison With Microseisms 492

[22] We have shown that infragravity waves gen- 493
erated by winter storms in the north Pacific Ocean 494
contribute to the source of the low-frequency 495
“hum” events observed in California and Japan. 496

[23] The nonlinear wave interactions that give rise 497
to infragravity waves are also responsible for the 498
generation of double-frequency microseisms [e.g., 499
Hasselmann, 1962, 1963; Longuet-Higgins, 1950], 500
which are themselves correlated with the wind 501
wave spectrum [e.g., *Babcock et al., 1994; Webb 502*
and Cox, 1986; Bromirski and Duennebieer, 2002], 503
and are known to be generated primarily locally 504
near the coast [e.g., *Haubrich and McCamy, 1969; 505*
Webb, 1998; Bromirski et al., 2005]. 506

[24] Therefore we next investigate the relationship 507
between microseisms, ocean storms and the low- 508
frequency “hum.” Even though there are two types 509
of microseisms, primary (at periods lower than 10 s) 510
and secondary, or “double-frequency,” at periods 511

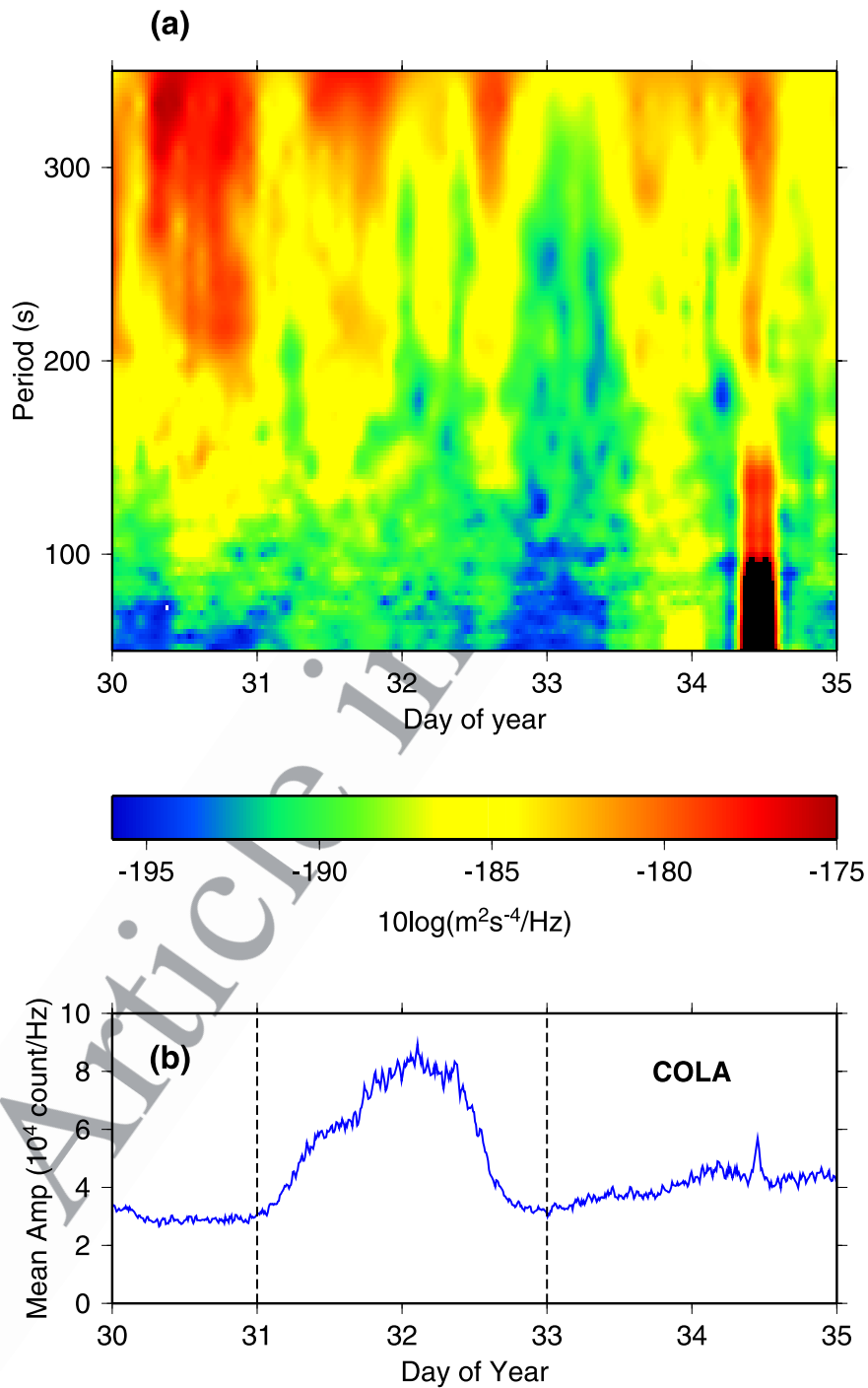


Figure 11. (a) Power spectral density (PSD) at COLA in Alaska. (b) Mean Fourier amplitude in the period range 2–25 s for COLA.

512 around 6–8 s [e.g., *Friedrich et al.*, 1998], and
513 their generation mechanisms are different [e.g.,
514 *Hasselmann*, 1963; *Webb*, 1998], the double-
515 frequency microseisms dominate the spectra and
516 we will only consider those in the discussion that
517 follows.

[25] We first computed mean Fourier amplitudes in 518
the microseismic period band (2 to 25 s) at indi- 519
vidual stations of BDSN and F-net for the time 520
interval 2000.031–2000.035. We used moving 521
windows of duration 30 mn, shifted by 10 mn. 522
We removed mean and trend before computing 523
Fourier amplitudes. We then compared them to 524

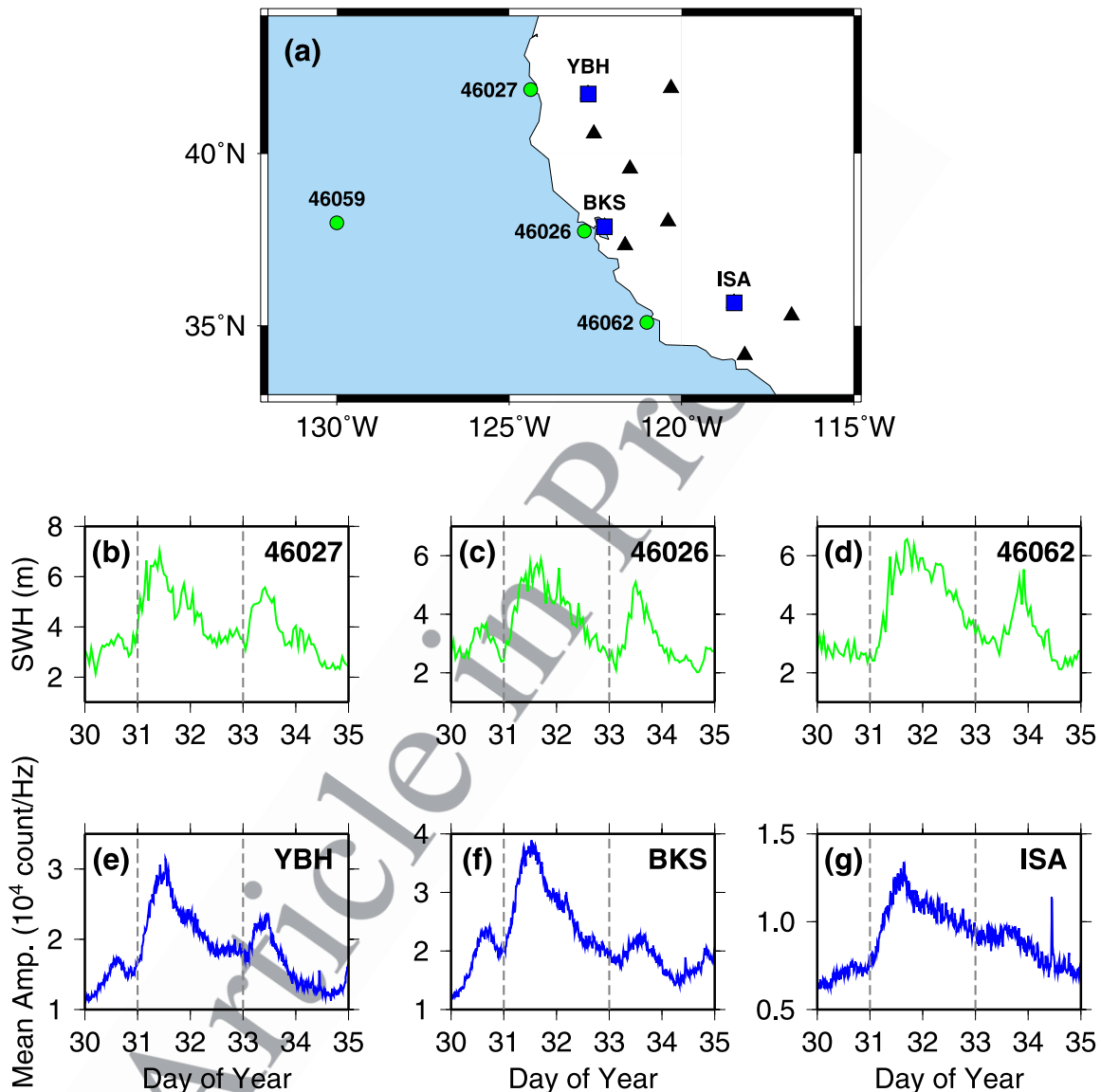


Figure 12. (a) Location map of BDSN and TerraScope stations (black triangle and blue squares) and buoys (green dots). Blue squares are seismic stations closest to the corresponding buoys. (b–d) Significant wave heights measured at buoy 46027, 46026, and 46052, respectively. (e–g) Mean Fourier amplitude (count/Hz) over the period range 2–25 s for YBH, BKS, and ISA.

525 near-by buoy data (Figures 12 and 13). Along the
526 coast of California (Figure 12), the mean seismic
527 amplitudes show the signatures of the two noise
528 events already discussed at low frequency (on days
529 2000.031 and 2000.033), which are also well
530 defined on the buoy data. The eastward moving
531 storm arrives first in northern and central Califor-
532 nia, as seen by the slight delay in its wave height
533 signature at buoy 46062 compared to the other two
534 buoys (see also the data from buoy 46059 on
535 Figure 7). The timing of the peak of microseismic
536 noise at the three stations and the fact that the
537 amplitude at station ISA is smaller by about a

factor of 3 than at BKS, indicate that the generation 538
of the microseisms occurs closer to the central and 539
northern California buoys. 540

[26] Unfortunately, only data for three buoys are 541
available around Japan for this time period. How- 542
ever, we note that the mean microseismic Fourier 543
amplitudes at the three seismic broadband stations 544
closest to the buoys show a good correlation with 545
SWH data (Figure 13). We also note that, contrary 546
to the observations in California, the timing and 547
shape of the microseismic amplitude variations is 548
different from that at “hum” frequencies, and 549

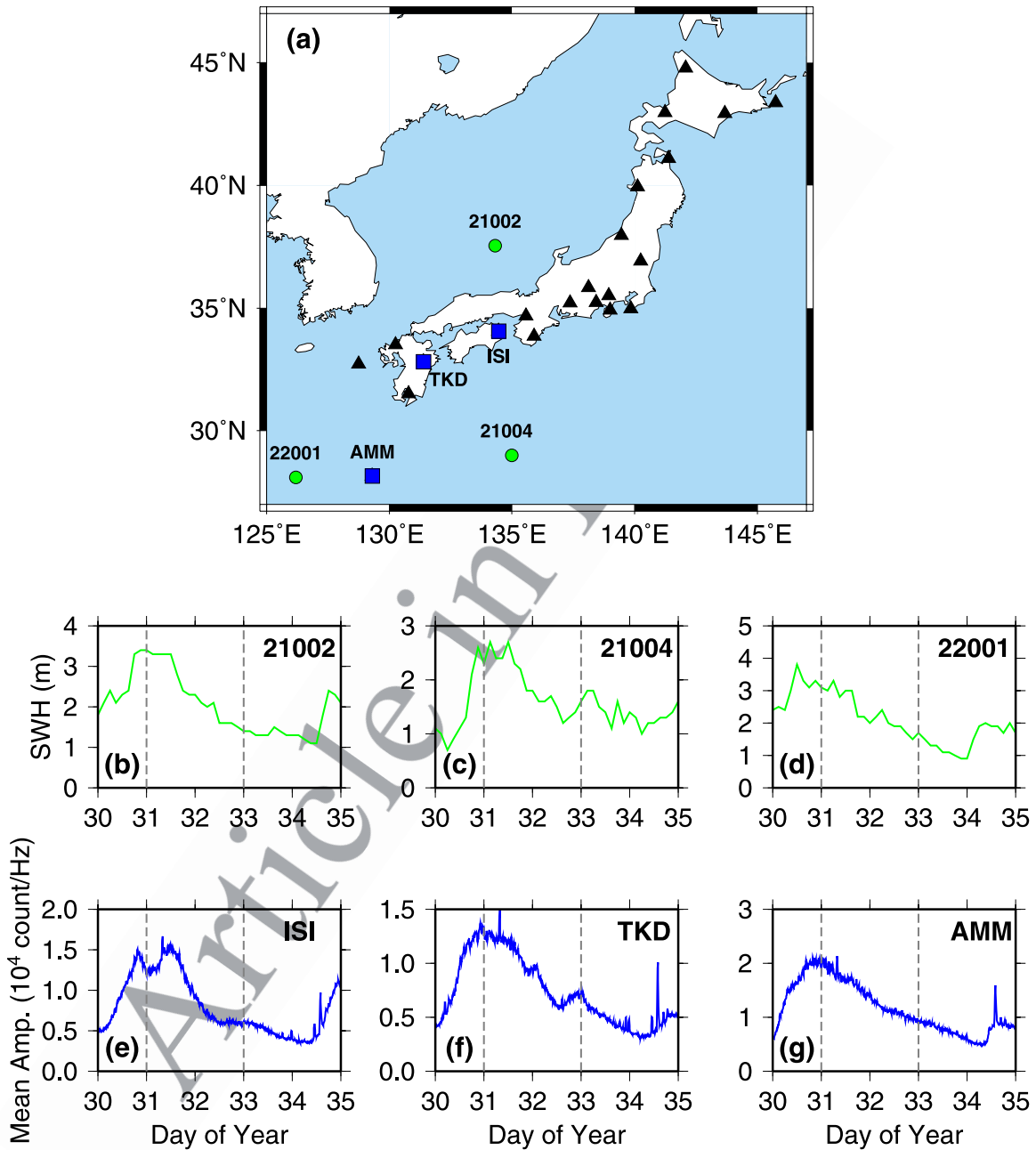


Figure 13. (a) Same as Figure 12 for F-net. (b–d) Same as Figures 12b, 12c, and 12d for 21002, 21004, and 22001, respectively. (e–g) Same as Figures 12e, 12f, and 12g for ISI, TKD, and AMM.

550 varies significantly with location of the station in
 551 the array (Figure 14), indicating that, in Japan, the
 552 sources of the microseismic noise and of the hum
 553 are distinct: the low-frequency noise is related to
 554 that observed on the eastern side of the Pacific
 555 (with a delay which we attribute to the propagation
 556 of infragravity waves across part of the Pacific
 557 Ocean), whereas the microseismic noise maximum
 558 occurs significantly earlier (on day 2000.030). In
 559 fact, the time histories of microseism energy at

stations within Japan differ and presumably depend
 on the location of each site relative to each storm
 track.

[27] To further investigate the relation between
 microseismic noise and the low-frequency hum,
 we need to be able to compare amplitude levels in
 the two frequency bands for long time intervals
 (e.g., a whole year). To do so effectively, we
 developed a data processing method that avoids

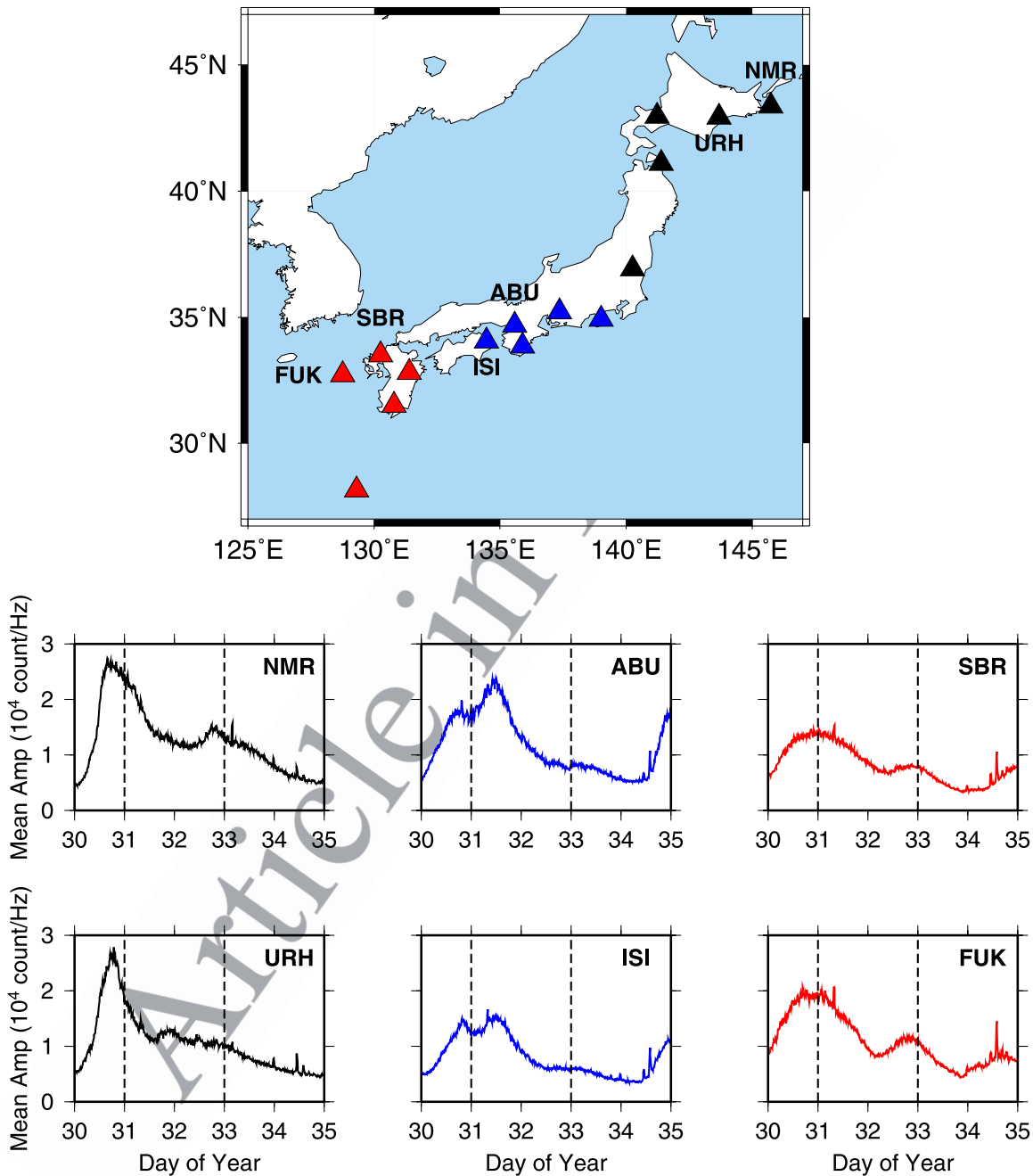


Figure 14. (top) Location map of seismic stations grouped by their locations in F-net. Different colors indicate different grouping. (bottom) Mean Fourier amplitude (count/Hz) over the period range 2–25 s for two selected stations in each group shown on the map at the top in black (left column), in blue (center column), and in red (right column). The variations in amplitude for all five stations (three of them are not shown) in the same group show similar overall trends.

569 eliminating the numerous time windows that are
570 contaminated by earthquakes.

571 [28] Removing the effect of earthquakes at low
572 frequencies is difficult to do precisely, due to the
573 presence of lateral heterogeneity in the Earth and

the relatively low attenuation. In order to minimize
574 their effects, we compute the minimum value, as a
575 function of time, in a sliding 1.5 day interval, of the
576 scaled MSA time series, using a moving time
577 window with a 6 hour shift. This effectively
578 removes some large amplitude peaks due to earth-
579

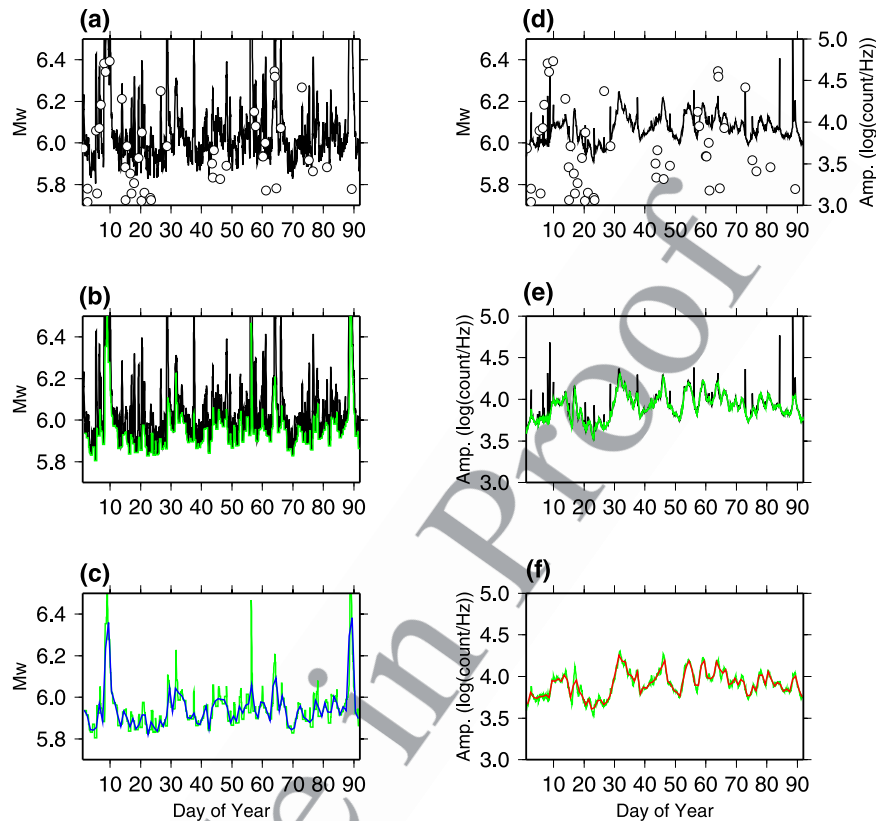


Figure 15. (a) Scaled long-period MSA, Gaussian filtered with center period of 240 s (blue curve) for BDSN. Circles indicate earthquakes. (b) Black curve: same as in Figure 15a. Green curve: minimum obtained after applying moving time window with duration of 1.5 days and 6 hour shift. (c) Green curve: same as in Figure 15b. Blue curve: after low-pass filtering with corner period of 1 day. (d) Mean Fourier amplitude over the microseismic band (2–25 s) averaged over 7 BDSN stations (black curve). Dots are earthquakes as in Figure 15a. (e) Black curve: same as in Figure 15d. Green curve: after removing large gradient peaks. (f) Green curve: same as in Figure 15e. Red curve: low-pass filtered with corner period of 1 day.

580 quakes, but not all. We then apply a low-pass filter
581 with a corner period of 1 day to the time series
582 obtained in the previous step. This further removes
583 most of the earthquake-related peaks, except for
584 those with the longest duration, corresponding to
585 the largest earthquakes (Figures 15a, 15b, and 15c).
586 We also compute the mean Fourier amplitude in the
587 microseismic band (2–25 s) for seven BDSN
588 stations. Here the contamination by large earth-
589 quakes is not as severe and we only remove those
590 points which correspond to large temporal gra-
591 dients. To do so, we empirically determined a
592 gradient threshold between two consecutive points
593 in the amplitude time series: if the measured
594 gradient is higher than the threshold, we remove
595 the end point and test the gradient value for
596 successive end points, until the gradient drops
597 below the threshold. Finally, we low-pass filter
598 the amplitude time series with a corner period of

1 day (Figures 15d, 15e, and 15f). This effectively 599
removes most of the earthquake signals. 600

[29] We compare the filtered “hum” and micro- 601
seism amplitude time series over a period of one 602
year, for each array. In the case of California 603
(BDSN), the level of low-frequency noise does 604
not vary systematically with time (Figure 16a), but 605
there is a seasonal variation in the microseismic 606
amplitude, with a minimum during northern hemi- 607
sphere summer time, as is also seen in the ocean 608
wave height data (Figure 16b). This indicates that 609
the sources of energy for the long-period and short- 610
period noise are different during the summer. The 611
variation in microseismic amplitude at BDSN sta- 612
tions is clearly related with ocean wave height 613
measured by local buoys (Figure 16b). We can 614
see a similar trend for F-net, but the correlation of 615
the variation in short-period amplitudes and ocean 616

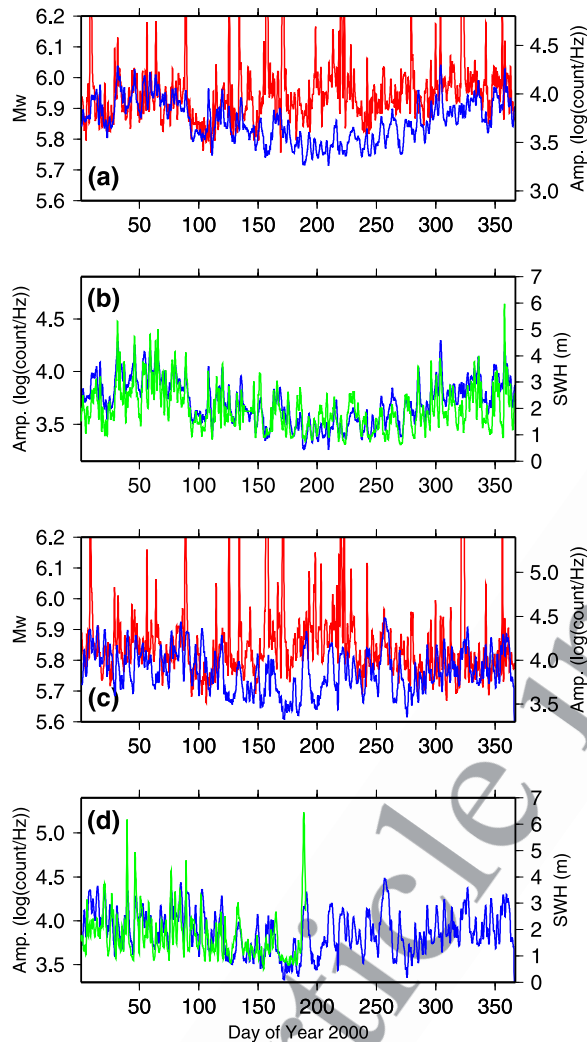


Figure 16. (a) Scaled long-period MSA (red) and short-period Fourier amplitude (blue), preprocessed as shown in Figure 15, for BDSN. The short-period mean Fourier amplitude was computed from 7 BDSN stations (BKS, CMB, MHC, MOD, ORV, WDC, and YBH). (b) Preprocessed short-period mean Fourier amplitudes (blue) for BDSN and significant wave height measured at buoy 46026 (green). The correlation coefficient between the two curves is 0.81. (c) Same as Figure 16a for 5 F-net stations near the eastern coast of Japan (AMM, ISI, NMR, TKD, and TMR). (d) Same as Figure 16b for F-net. Significant wave height data measured at buoy 21004 (green) is not available after day 190 in 2000. Large peaks in short-period mean Fourier amplitude and ocean waves during summer may be coming from the typhoon. The correlation coefficient between the two curves for the first part of the year is 0.58.

617 wave data is weaker than in the case of BDSN
618 (Figures 16c and 16d).

619 [30] Removing the time periods contaminated by
620 the largest events, and restricting our analysis to

northern hemisphere winter (January to March and
October to December), we compute the correlation
coefficients between the low-frequency and high-
frequency filtered noise time series, for three con-
secutive years, at BDSN. Correlation coefficients
are significant, between 0.39 and 0.60 (Figure 17).
This indicates that in the winter, both the low-
frequency hum and the microseismic noise ob-
served at BDSN are generated locally. On the other
hand, the corresponding correlation coefficients
for F-net are generally much lower: for the first
3 months of each year, respectively: -0.11 , (N/A)
and 0.21 ; for the last 3 months of each year,
respectively: 0.22 , -0.02 , 0.30 .

[31] The correlation between the hum and micro-
seismic noise at BDSN during the winter is com-
patible with a common generation mechanism for
both types of seismic noise, involving nonlinear
interactions between surface ocean waves giving
rise, on the one hand, to double-frequency micro-
seisms, and on the other, to infragravity waves
[e.g., *Hasselmann*, 1962]. The fact that the corre-
lation is somewhat weaker at F-net is in agreement
with our proposed scenario, in which the dominant
effect is that of storms moving from West to East
across the Pacific and reaching the west coast of
North America to produce low-frequency seismic
“hum.”

5. Conclusions

[32] We have made progress in clarifying the
mechanism of generation of continuous free oscil-
lations, based on the observations for a time
interval free of earthquakes during which two large
long-period noise events are present in the MSA at
BDSN and F-net. We have shown that these events
can be related to a particular winter storm system.

[33] A perturbation in the atmosphere, typically a
winter storm moving eastward across the north
Pacific basin, generates short-period ocean waves.
As the storm reaches the north-American coast, the
nonlinear interaction between ocean waves gener-
ates long-period infragravity waves, some of which
convert locally to long-period seismic energy, and
others propagate long distance across the ocean
basin and couple to the seafloor near northeastern
coasts. The resulting long-period seismic waves
propagate over the globe and give rise to the
“hum.” In particular, we were able to track the
seismic energy generated off-shore California by
the storm considered on day 2000.031, throughout
the North American continent.

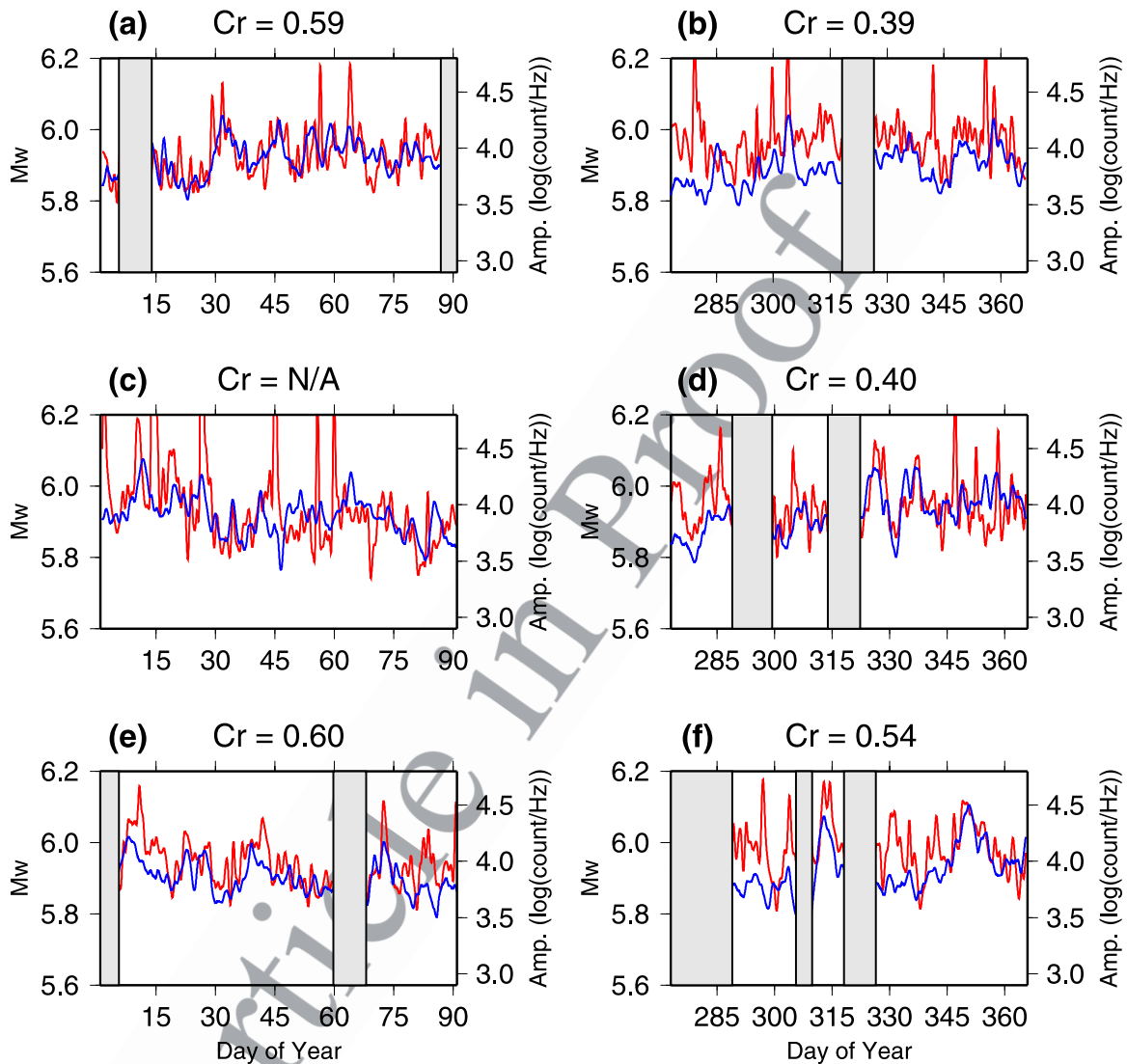
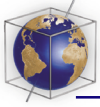


Figure 17. (a) Comparison between preprocessed scaled long-period MSA (red) and short-period mean Fourier amplitudes (blue) for the first three months of 2000. Time windows strongly contaminated by earthquakes are shaded in gray. Corresponding correlation coefficient is shown in the plot. (b) Same as Figure 17a for the last three months in 2000. (c–d) Same as Figures 17a and 17b for 2001. For Figure 17c, correlation coefficient is not computed because of significant contamination from earthquakes throughout the time period considered. (e–f) Same as Figures 17a and 17b for 2002.

672 [34] The directionality of the “hum” radiation sug- 683
 673 gested by our data needs to be further characterized, 684
 674 in particular for the benefit of studies of structure 685
 675 based on the analysis of noise cross-correlations 686
 676 [e.g., Shapiro *et al.*, 2005], at least at low frequen- 687
 677 cies. Indeed, the sources of low-frequency seismic 688
 678 noise can no longer be considered as uniformly 689
 679 distributed either in time, or in space.

680 [35] The annual fluctuations of long- (hum band) 690
 681 and short- (microseism band) period seismic ampli- 691
 682 tudes at BDSN and F-net show quite different 692

683 features. We can clearly see the seasonal change 684
 685 in amplitude in the microseism band (2–25 s) with 686
 687 a minimum during northern hemisphere summer, 688
 689 whereas the amplitude in the hum band (here 689
 690 considered at ~240s) does not show clear seasonal 691
 692 variations. We also observed a significant correla- 693
 694 tion between seismic amplitudes at BDSN in the 694
 695 microseism and hum bands during northern hemi- 696
 697 sphere winter. We had previously documented that 697
 698 the source of the hum observed at BDSN and F-net 698
 699 shifts from the northern Pacific to the southern 699
 700 oceans between winter and summer, so that the 700

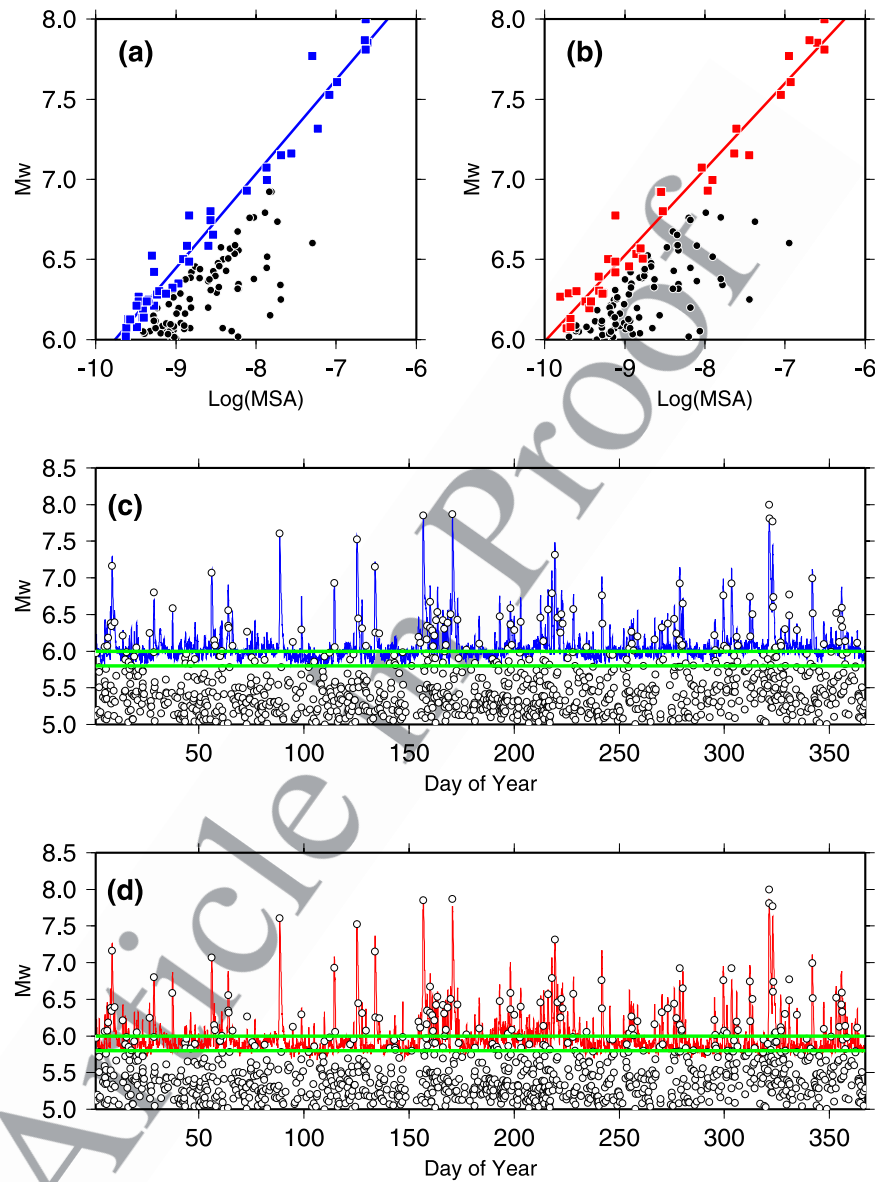


Figure A1. Estimation of the level of low-frequency background noise at ~ 240 s (i.e., the hum) for the year 2000. (a) Moment magnitudes versus associated maxima in MSA for BDSN. The MSA is shown after applying a moving average over a window of 6 hours with 1 hour offset. Results do not significantly change if no moving average is applied. Black dots indicate all seismic events during the year, and solid squares indicate selected maxima which are not contaminated by later Rayleigh wave trains from other large events. The best fitting line is computed using only the data indicated by blue squares. The best fitting line is used to scale MSA to match the plausible level of the background noise. (b) Same as Figure A1a for F-net. Red squares are selected maxima. (c) Scaled MSA (blue) for BDSN. Open circles represent all large events during the year 2000. The levels corresponding to M_w 5.75 and M_w 6 are highlighted with green lines. (d) Same as Figure A1c for F-net (red).

695 sources are more “local” in the winter than in the
696 summer. In contrast, microseisms propagate less
697 efficiently at large distances, so the source is
698 primarily local. These observations are in agree-
699 ment with a common mechanism for the simulta-
700 neous generation of short- and long-period seismic

noise near the California coast, as inferred from 701
theoretical studies. 702

Appendix A 703

[36] We estimate the background level of the low- 704
frequency seismic energy by determining a scaling 705

706 factor between the observed peak amplitudes (from
707 the MSA at 240 s), and the moment magnitudes of
708 the corresponding earthquakes ($M_w > 6.0$), as listed
709 in the Harvard CMT catalog [Dziewonski and
710 Woodhouse, 1983].

711 [37] Since we know the location of both the
712 array and each earthquake, as well as the event
713 origin time, we can calculate the theoretical onset
714 time of the R1 train at the center of the array
715 and select only those peaks that correspond to
716 the arrival time of the R1 train. However, the
717 selection of R1 peaks is made difficult by the
718 presence of secondary peaks corresponding to
719 later arriving Rayleigh wave trains from the
720 previous larger earthquakes (R2,R3...). When
721 such secondary peaks are present, the
722 corresponding seismic amplitude is significantly
723 larger than estimated, on average, based on the
724 magnitude of the earthquake considered. When
725 estimating the scaling factor, and to reduce
726 contamination due to large previous events, we
727 therefore discard those peaks from the data set
728 that have relatively high amplitude for a given
729 magnitude level. This means that, when applying
730 this scaling factor, our estimate of the hum level
731 is maximum (Figures A1a and A1b). Since we
732 ignore the effects of geometrical spreading, at-
733 tenuation during propagation, as well as radiation
734 pattern, this is a very crude estimate. However,
735 the estimated noise background level is consis-
736 tent with what has been previously reported
737 (Figures A1c and A1d) from the analysis of free
738 oscillation data (e.g., M_w 5.75 [Ekström, 2001];
739 M 6.0 [Tanimoto and Um, 1999]).

740 Acknowledgments

741 [38] We wish to thank the staff of BDSN, F-net, JMA, NOAA
742 for providing high-quality and continuous seismic and ocean
743 buoy data. We thank Spahr Webb and an anonymous reviewer
744 for helpful comments. Berkeley Seismological Laboratory
745 contribution 06-XYZ.

747 References

748 Babcock, J. M., B. A. Kirkendall, and J. A. Orcutt (1994),
749 Relationships between ocean bottom noise and the environ-
750 ment, *Bull. Seismol. Soc. Am.*, *84*, 1991–2007.
751 Bromirski, P. D., and F. K. Duennebieer (2002), The near-coastal
752 microseism spectrum: Spatial and temporal wave climate re-
753 lationships, *J. Geophys. Res.*, *107*(B8), 2116, doi:10.1029/
754 2001JB000265.
755 Bromirski, P. D., F. Duennebieer, and R. A. Stephen (2005),
756 Mid-ocean microseisms, *Geochem. Geophys. Geosyst.*, *6*,
757 Q04009, doi:10.1029/2004GC000768.
758 Dolenc, D., B. Romanowicz, D. Stakes, P. McGill, and
759 D. Neuhauser (2005a), Observations of infragravity waves at

the Monterey ocean bottom broadband station (MOBB), *Geo-* 760
chem. Geophys. Geosyst., *6*, Q09002, doi:10.1029/ 761
2005GC000988. 762
Dolenc, D., B. Romanowicz, D. Stakes, P. McGill, and 763
D. Neuhauser (2005b), Observations of infragravity waves 764
at the Monterey ocean bottom broadband station (MOBB), 765
Eos Trans. AGU, *85*(52), Fall Meet. Suppl., Abstract 766
S34B-05. 767
Dziewonski, A. M., and D. L. Anderson (1981), Preliminary 768
reference Earth model, *Phys. Earth Planet. Inter.*, *25*, 297– 769
356. 770
Dziewonski, A. M., and J. H. Woodhouse (1983), Studies 771
of the seismic source using normal-mode theory, in 772
Earthquakes: Observation, Theory, and Interpretation: 773
Notes From the International School of Physics “Enrico 774
Fermi” (1982: Varenna, Italy), edited by H. Kanamori 775
and E. Boschi, pp. 45–137, Elsevier, New York. 776
Ekström, G. (2001), Time domain analysis of Earth’s long- 777
period background seismic radiation, *J. Geophys. Res.*, 778
106, 26,483–26,493. 779
Ekström, G., and S. Ekström (2005), Correlation of Earth’s 780
long-period background seismic radiation with the height 781
of ocean waves, *Eos Trans. AGU*, *86*(52), Fall Meet. Suppl., 782
Abstract S34B-02. 783
Elgar, S., T. H. C. Herbers, M. Okihiro, J. Oltman-Shay, 784
and R. T. Guza (1992), Observations of infragravity 785
waves, *J. Geophys. Res.*, *97*, 15,573–15,577. 786
Friedrich, A., F. Krüger, and K. Klinge (1998), Ocean- 787
generated microseismic noise located with the Gräfenberg 788
array, *J. Seismol.*, *2*, 47–64. 789
Hasselmann, K. (1962), On the non-linear energy transfer in a 790
gravity-wave spectrum, Part I. General theory, *J. Fluid 791*
Mech., *12*, 481–500. 792
Hasselmann, K. (1963), A statistical analysis of the generation 793
of microseisms, *Rev. Geophys.*, *1*, 177–210. 794
Haubrich, R. A., and K. McCamy (1969), Microseisms: Coastal 795
and pelagic sources, *Rev. Geophys.*, *7*, 539–571. 796
Herbers, T. H. C., S. Elgar, and R. T. Guza (1994), Infragrav- 797
ity-frequency (0.005–0.05 Hz) motions on the shelf, Part I: 798
Forced waves, *J. Phys. Oceanogr.*, *24*, 917–927. 799
Herbers, T. H. C., S. Elgar, and R. T. Guza (1995a), Generation 800
and propagation of infragravity waves, *J. Geophys. Res.*, 801
100, 24,863–24,872. 802
Herbers, T. H. C., S. Elgar, R. T. Guza, and W. C. O. Reilly 803
(1995b), Infragravity-frequency (0.005–0.05 Hz) motions on 804
the shelf, Part II: Free waves, *J. Phys. Oceanogr.*, *25*, 1063– 805
1079. 806
Louquet-Higgins, M. S. (1950), A theory of the origin of 807
microseisms, *Philos. Trans. R. Soc. London, Ser. A*, *243*, 808
1–35. 809
Louquet-Higgins, M. S., and R. W. Stewart (1962), Radiation 810
stress and mass transport in surface gravity waves with ap- 811
plication to “surf beats,” *J. Fluid Mech.*, *13*, 481–504. 812
Munk, W. (1949), Surf beats, *Eos Trans. AGU*, *30*, 849–854. 813
Munk, W., F. Snodgrass, and F. Gilbert (1964), Long waves on 814
the continental shelf: An experiment to separate trapped and 815
leaking modes, *J. Fluid Mech.*, *20*, 529–554. 816
Nawa, K., N. Suda, Y. Fukao, T. Sato, Y. Aoyama, and 817
K. Shibuya (1998), Incessant excitation of the Earth’s free 818
oscillations, *Earth Planets Space*, *50*, 3–8. 819
Nishida, K., and Y. Fukao (2004), Spatial variations of excita- 820
tion amplitudes of Earth’s background free oscillations, *Eos 821*
Trans. AGU, *84*(46), Fall Meet. Suppl., Abstract S31B-1068. 822
Nishida, K., and N. Kobayashi (1999), Statistical features of 823
Earth’s continuous free oscillations, *J. Geophys. Res.*, *104*, 824
28,731–28,750. 825

- 826 Nishida, K., N. Kobayashi, and Y. Fukao (2000), Resonant
827 oscillations between the solid Earth and the atmosphere,
828 *Science*, 287, 2244–2246.
- 829 Okihiro, M., R. T. Guza, and R. J. Seymour (1992), Bound
830 infragravity waves, *J. Geophys. Res.*, 97, 11,453–11,469.
- 831 Rhie, J., and B. Romanowicz (2003), Detection and location of
832 long period surface wave energy sources, *Eos Trans. AGU*,
833 84(46), Fall Meet. Suppl., Abstract S42E-0211.
- 834 Rhie, J., and B. Romanowicz (2004), Excitation of Earth's
835 continuous free oscillations by atmosphere-ocean-seafloor
836 coupling, *Nature*, 431, 552–556.
- 837 Roult, G., and W. Crawford (2000), Analysis of 'background'
838 free oscillations and how to improve resolution by subtract-
839 ing the atmospheric pressure signal, *Phys. Earth Planet. In-
840 ter.*, 121, 325–338.
- 841 Shapiro, N. M., M. Campillo, L. Stehly, and M. H. Ritzwoller
842 (2005), High-resolution surface-wave tomography from amb-
843 bient seismic noise, *Science*, 307, 1615–1618.
- 844 Suda, N., K. Nawa, and Y. Fukao (1998), Earth's background
845 free oscillations, *Science*, 279, 2089–2091.
- 846 Sutton, G. H., W. G. McDonald, D. D. Prentiss, and S. N.
847 Thanos (1965), Ocean-bottom seismic observatories, *Proc.
848 IEEE*, 53, 1909–1921.
- 849 Tanimoto, T. (2003), Jet stream, roaring ocean waves, and
850 ringing Earth, *Eos Trans. AGU*, 84(46), Fall Meet. Suppl.,
851 Abstract S12F-04.
- Tanimoto, T. (2005), The oceanic excitation hypothesis for the
continuous oscillations of the Earth, *Geophys. J. Int.*, 160,
276–288.
- Tanimoto, T., and J. Um (1999), Cause of continuous oscilla-
tions of the Earth, *J. Geophys. Res.*, 104, 28,723–28,739.
- Tolman, H. L. (1999), User manual and system documentation
of WAVEWATCH III, version 1.18, *Tech. Rep. Ocean Mod-
eling Branch Contrib. 166*, NOAA/NWS/NCEP, Silver
Spring, Md..
- Tucker, M. J. (1950), Surf beats: Sea waves of 1 to 5 min
period, *Proc. R. Soc. London, Ser. A*, 207, 565–573.
- Watada, S., and G. Masters (2001), Oceanic excitation of the
continuous oscillations of the Earth, *Eos Trans. AGU*,
82(47), Fall Meet. Suppl., Abstract S32A-0620.
- Webb, S. (1998), Broadband seismology and noise under the
ocean, *Rev. Geophys.*, 36, 105–142.
- Webb, S. C., and C. S. Cox (1986), Observations and modeling
of seafloor microseisms, *J. Geophys. Res.*, 91, 7343–7358.
- Webb, S., X. Zhang, and W. Crawford (1991), Infragravity
waves in the deep ocean, *J. Geophys. Res.*, 96, 2723–
2736.
- Wielandt, E., and J. M. Steim (1986), A digital very-broad-
band seismograph, *Ann. Geophys., Ser. B*, 4, 227–232.
- Wielandt, E., and G. Streckeisen (1982), The leaf-spring
seismometer: Design and performance, *Bull. Seismol. Soc.
Am.*, 72, 2349–2367.

Article in Progress